

#### **OPEN ACCESS**

EDITED BY Sunil Gc, North Dakota State University, United States

REVIEWED BY
Weibin Guo,
Hefei Institutes of Physical Science, Chinese
Academy of Sciences (CAS), China
Jialin Yu,
Peking University, China
Hongxiang Xue,
Anhui Science and Technology University,
China

\*CORRESPONDENCE
Maocheng Zhao
mczhao@njfu.edu.cn

RECEIVED 04 September 2025 ACCEPTED 29 October 2025 PUBLISHED 28 November 2025

#### CITATION

Zuo Z, Zhao M, Qi L, Wu B, Zou H, Xie W, Ye Q, Zhou C and Zhang K (2025) Hyperspectral inversion model of ginkgo leaf yield prediction based on machine learning. *Front. Plant Sci.* 16:1698830. doi: 10.3389/fpls.2025.1698830

#### COPYRIGHT

© 2025 Zuo, Zhao, Qi, Wu, Zou, Xie, Ye, Zhou and Zhang. This is an open-access article distributed under the terms of the Creative Commons Attribution License (CC BY). The use, distribution or reproduction in other forums is permitted, provided the original author(s) and the copyright owner(s) are credited and that the original publication in this journal is cited, in accordance with accepted academic practice. No use, distribution or reproduction is permitted which does not comply with these terms.

# Hyperspectral inversion model of ginkgo leaf yield prediction based on machine learning

Zheng Zuo<sup>1</sup>, Maocheng Zhao<sup>1\*</sup>, Liang Qi<sup>1,2</sup>, Bin Wu<sup>1</sup>, Hongyan Zou<sup>1</sup>, Weijun Xie<sup>1</sup>, Qiaolin Ye<sup>3</sup>, Chi Zhou<sup>1</sup> and Kai Zhang<sup>1</sup>

<sup>1</sup>College of Mechanical and Electronic Engineering, Nanjing Forestry University, Nanjing, China, <sup>2</sup>Jinpu Research Institute, Nanjing Forestry University, Nanjing, China, <sup>3</sup>College of Information Science and Technology, Nanjing Forestry University, Nanjing, China

**Introduction:** The yield of ginkgo biloba leaves serves as a critical indicator for assessing their growth and health status. However, current assessment methods primarily rely on manual harvesting and weighing, which are time-consuming, labor-intensive, inefficient, and costly.

Methods: To address these limitations, this study designed an algorithm-based vield estimation approach: by employing airborne hyperspectral imaging technology at a research base to replace traditional manual measurements, a canopy hyperspectral dataset and Region of Interest Pixel (ROP) sets were constructed. Five preprocessing methods, Multiplicative Scatter Correction (MSC), Standard Normal Variate (SNV), Savitzky-Golay (SG), First Derivative (FD), and Standard Scaling (SS), were employed to develop Partial Least Squares Regression (PLSR) models, identifying the optimal hyperspectral data preprocessing approach. The optimal preprocessing model was subsequently integrated with Particle Swarm Optimization (PSO), Successive Projections Algorithm (SPA), Principal Component Analysis (PCA), Least Absolute Shrinkage and Selection Operator (LASSO), Competitive Adaptive Reweighted Sampling (CARS) and Particle Swarm Attention Mechanism Algorithm (PSAMA) for feature band selection. Traditional spectral vegetation indices were refined through random forest stepwise regression and spectral index correlation analysis, ultimately determining Soil-Adjusted Vegetation Index (SAVI), Modified Soil-Adjusted Vegetation Index (MSAVI), Normalized Difference Red Edge Index (NDRE), Structure Insensitive Pigment Index (SIPI) as the final indices. The selected spectral bands and vegetation indices were then incorporated with PLSR, Random Forest (RF), K-Nearest Neighbors Regression (KNNR), Long Short-Term Memory (LSTM), Support Vector Regression (SVR), Bidirectional LSTM (BiLSTM), and BiLSTM- Grid SearchCV (BiLSTM-GS) machine learning models for yield prediction.

**Results:** Results demonstrated that the SNV-PLSR model achieved superior performance ( $R_p^2 = 0.7831$ ,  $RMSE_p = 0.0325$ ). The optimal SNV- (SAVI - MSAVI - NDRE - SIPI - ROP) - (BiLSTM-GS) model, combining PSAMA-selected feature bands with vegetation index and ROP, yielded outstanding prediction accuracy ( $R_p^2 = 0.8795$ ,  $RMSE_p = 0.1021$ ).

**Discussion:** This airborne hyperspectral canopy-based estimation technology provides an accurate, non-destructive solution for monitoring ginkgo leaf yield in field cultivation.

KEYWORDS

hyperspectral imaging, analysis, spectral index, ginkgo biloba leaves, non-destructive solution

#### 1 Introduction

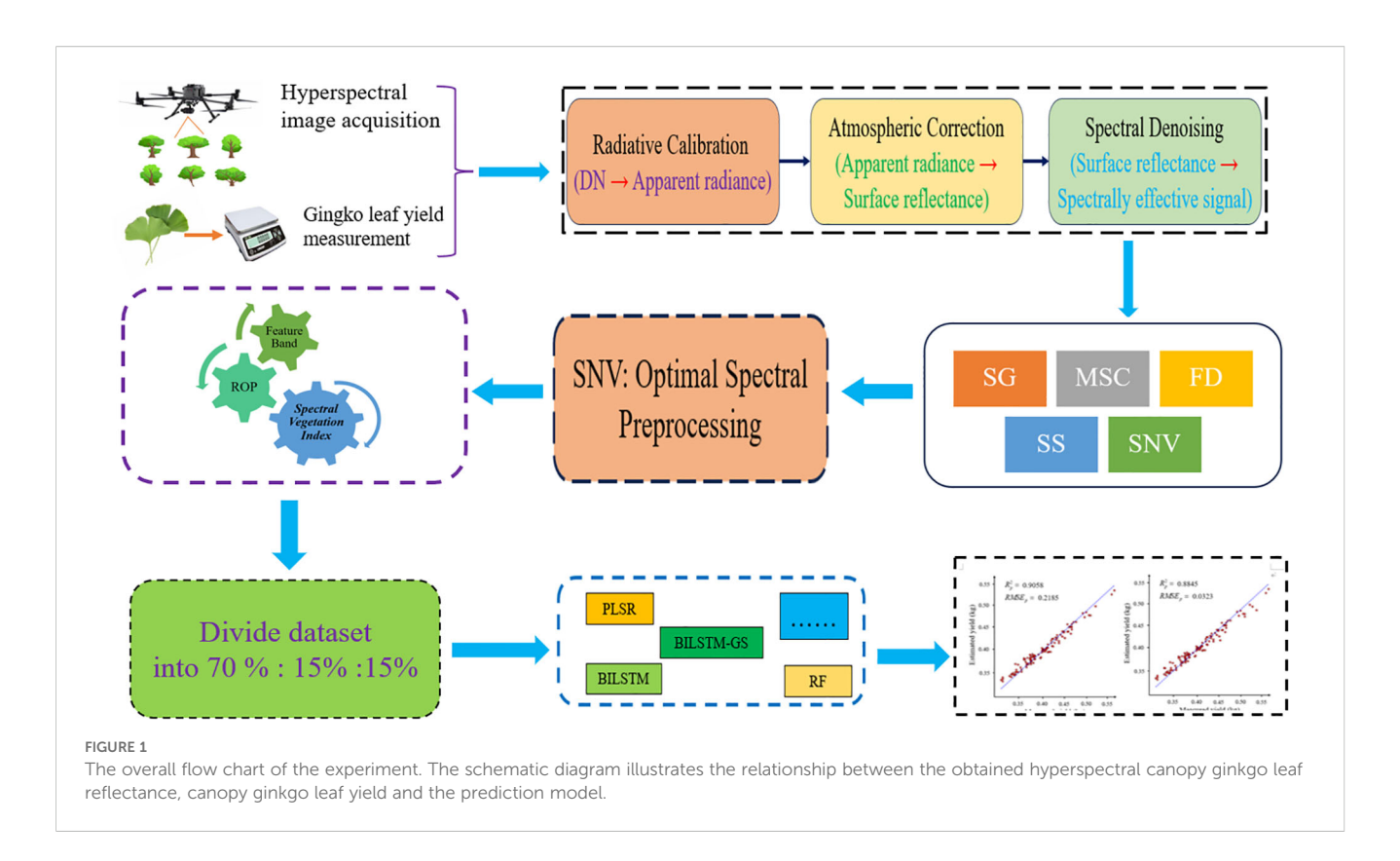
As an economically important medicinal plant, Ginkgo biloba is cultivated worldwide for its leaves, which serve as the primary raw material for pharmaceutical and health products (Liu et al., 2022; Lu et al., 2024). According to modern pharmacological research, Ginkgo biloba has a promoting effect on protecting nerve cells, anti-oxidation and scavenging free radicals at the body (Vitor et al., 2023; Sen et al., 2025). In the growth process of Ginkgo biloba, its yield plays a vital role, which is one of the important factors that determine the growth of Ginkgo biloba (Li et al., 2024). Traditional ginkgo leaf yield test methods, such as scale weighing method, are usually only suitable for small plot experiments, and there are problems such as time-consuming, laborious operation, and destruction of plant growth. To address the above problems, researchers have proposed a new detection method, that is, airborne hyperspectral canopy ginkgo leaf image to predict ginkgo leaf yield. This method not only saves time, effort and protects plant growth, but also is suitable for the detection of largescale plots.

Research on the detection of plant yield based on hyperspectral technology has gradually increased. Different plant yield estimation models are established mainly through hyperspectral image data preprocessing (Jin et al., 2023), feature band selection, and machine learning model algorithms (Li et al., 2025; Yan et al., 2025). For example, Qin et al. (2025) used the ASD hyperspectral sensor to collect the hyperspectral yield data of apple tree canopy in the whole growth stage of spring and autumn. First, the convolution Savitzky-Golay (SG) was used to preprocess the hyperspectral data. Second, the sensitive bands in hyperspectral data were screened by Genetic Algorithm (GA) and Successive Projections Algorithm (SPA). Finally, the selected bands were combined with machine learning models such as PLSR, RF, and XGBoost to predict the hyperspectral yield data of apple trees collected in spring and autumn. The results showed that the data collected in autumn performed better in prediction performance. The best model combination was SG-(VISSA-CARS) -RF, with  $R^2$  of 0.78 and RMSE of 6.03 in the validation set.

Burglewski et al. (2024) used a hyperspectral imager to collect spectral data of corn straw, aiming to estimate the yield of corn as silage. In the study, seven spectral bands including red edge bands and multiple near-infrared bands were used to predict the yield combined with the Support Vector Regression (SVR) model. The results show that the method can achieve more than 90% prediction accuracies (Mao et al., 2024). predicted wheat yield and yield loss under water and nitrogen stress using hyperspectral remote sensing data and Partial Least Squares Regression (PLSR) models. In this study, researchers paired canopy hyperspectral data from the same location, at the same growth stage but under different stress conditions with yield data to form a data combination for verifying the performance of the model. The results showed that compared with the traditional PLSR model, the MRE-PLSR model significantly improved the prediction accuracy, and the Pearson correlation coefficient increased by an average of 14.5%.

Ceriani et al. (2025) integrated hyperspectral and LiDAR spaceborne data to estimate forest volume and biomass in mountainous regions. By combining LiDAR-derived metrics (e.g., canopy height) with hyperspectral indices, they used machine learning models like Random Forest (RF) and Support Vector Regression (SVR) to predict aboveground biomass and forest volume. The results showed that the fusion of both datasets improved accuracy, with an  $R^2$  value above 0.85 and a 20% reduction in root mean square error. This highlights the potential of using integrated remote sensing data for large-scale forest assessments. Miettinen et al. (2024) utilized hyperspectral imaging to reveal the spatiotemporal dynamics of chlorophyll and carotenoids in Scots pine under water stress. Among the multiple machine learning models evaluated, the Random Forest Regression (RFR) model demonstrated the best predictive performance, with predictions most closely aligned with measured values and the lowest Root Mean Square Error (RMSE). Tougas et al. (2025)captured the weak spectral features of the early stage of beech tree disease by hyperspectral imaging technology, and systematically evaluated the classification performance of various machine learning models. The results showed that the random forest (RF) model performed best in this task, with a classification accuracy of 85%, which was significantly ahead of other models, confirming the effectiveness and application potential of hyperspectral technology combined with RF model in early diagnosis of forest diseases.

While previous studies have extensively applied hyperspectral remote sensing to crop monitoring, research on ginkgo leaf yield prediction by integrating hyperspectral technology with machine



learning remains relatively scarce. Building on existing methodologies, this study employs airborne hyperspectral imaging and electronic weighing for efficient and non-destructive data acquisition of ginkgo leaf spectra and yield. The proposed approach is operationally straightforward, time-efficient, and suitable for field applications. The main innovations of this work are summarized as follows:

- 1. To achieve the efficient screening of hyperspectral features, an attention mechanism model is integrated into the Particle Swarm Optimization (PSO) algorithm, leading to the construction of the PSAMA optimization algorithm.
- The integration of optimally selected feature bands, refined spectral vegetation indices, and ginkgo canopy Region of Interest Pixel (ROP) sets can significantly enhance both the accuracy and reliability of yield prediction models.
- A novel SNV- (SAVI MSAVI NDRE SIPI ROP) -(BiLSTM-GS) prediction model is proposed, which achieves excellent detection performance through innovative architecture design and optimization training.

#### 2 Materials and methods

The overall workflow of this study is illustrated in Figure 1, which outlines the complete process of hyperspectral data acquisition, preprocessing, feature extraction, and model construction for Ginkgo biloba leaf yield estimation. This schematic provides an

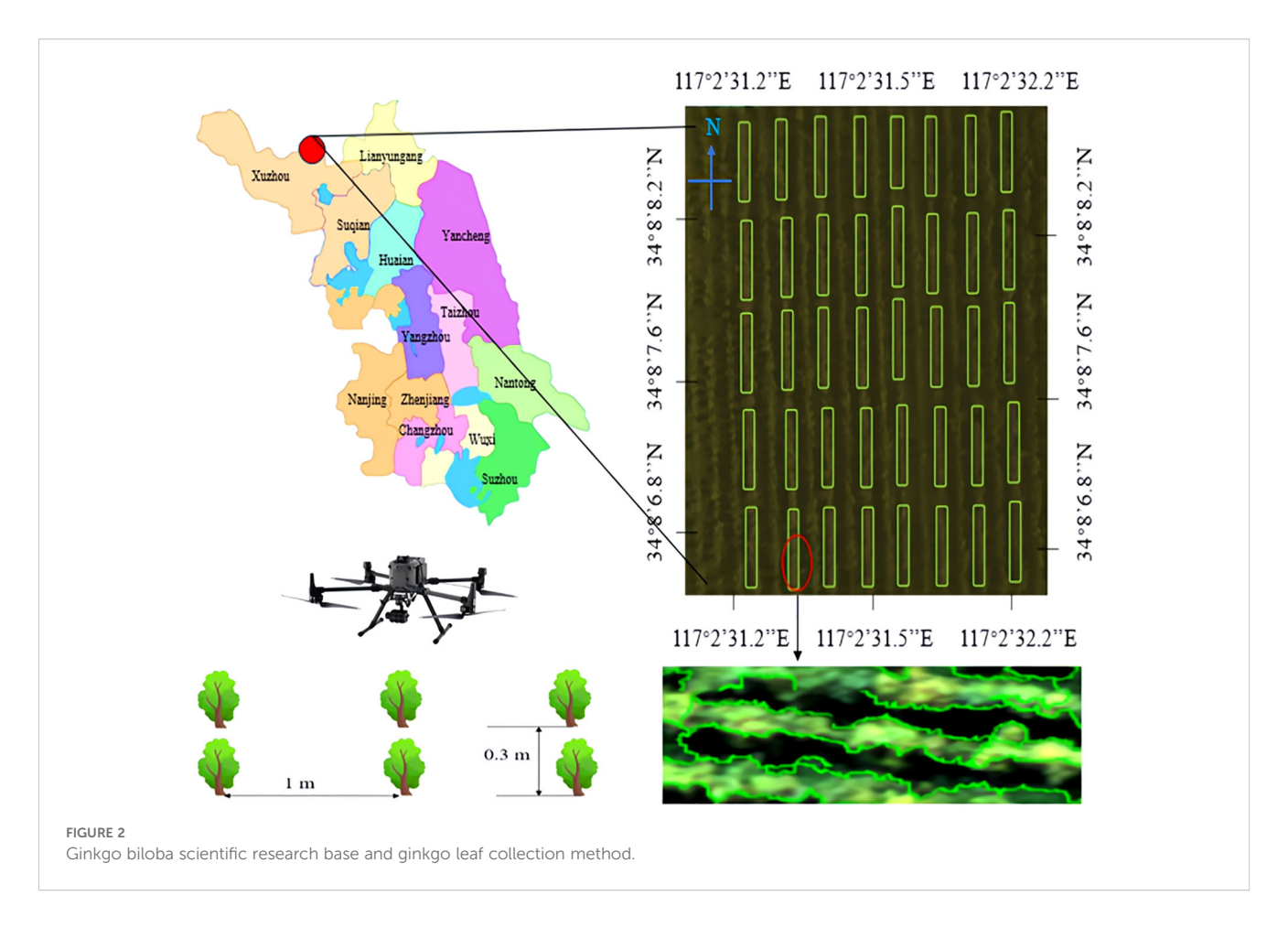
overview of how canopy hyperspectral reflectance, ginkgo leaf yield, and the prediction model are interrelated.

#### 2.1 Experimental site and period

Hyperspectral remote sensing images of Ginkgo biloba canopy were acquired for yield acquisition. The experimental site was Xuzhou Changrong Agricultural Development Co., Ltd. (34°8  $^{\circ}$  42'N, 117°2  $^{\circ}$ 45'E). A total of 10,000 Ginkgo biloba trees were planted in the scientific research base, covering a plot size of 0.8  $\times$  4  $\rm m^2$ . The experimental involved three-year-old ginkgo trees cultivated at the scientific research base. The trees were spaced 1 m between rows and 0.3 m between plants. Figure 2 shows the geographical location of the experimental site and the contour characteristics of the ginkgo tree canopy.

## 2.2 Hyperspectral remote sensing image acquisition of canopy ginkgo leaves

In this study, ginkgo leaves in the experimental site were selected as the research object, and the remote sensing data of ginkgo leaf canopy were obtained by using an airborne hyperspectral imaging system (GaiaSky-mini3-VN, Double-profit Hepu Technology Co., Ltd., China). The hyperspectral imaging system used in this study has a spectral response range of 400  $\sim$  1000 nm, equipped with 224 spectral channels and 1024 spatial channels, which can achieve a spatial resolution of 1024  $\times$  1003



pixels and a spectral resolution of 5 nm. The lens carried by the imaging system has an optical resolution of 16 nm, and the overall power consumption of the system is 45 W. The UAV was used as the data acquisition platform, and the flight height was fixed at 50 m (DJI M350, DJI Innovation Technology Co., Ltd., China). During data acquisition, the drone maintains a hover for 10 s, and continuous image acquisition is performed through the built-in push-scanning mode of the hyperspectral imager to ensure spatial continuity and spectral consistency of the data. The hyperspectral canopy images of ginkgo leaves were acquired on July 19,2024 and September 15,2024. The weather was sunny, with temperatures of 30 °C and 24 °C, relative humidities of 75% and 68%, and wind speeds of 8.6 km/h and 6.4 km/h, respectively.

#### 2.3 Field measurement of ginkgo leaf yield

From July 19 to 26, 2024 and from September 15 to 21, 2024, the laboratory team successfully completed the acquisition of hyperspectral images of ginkgo tree canopy leaves at the research base. Upon concluding the image collection, the team grouped the leaves from every twenty ginkgo trees into one sample unit, obtaining a total of 200 sample datasets. Subsequently, an electronic balance (manufactured by Kunshan Toptech Electronic Co., Ltd., featuring functions such as counting, pricing, and weighing) was used to

precisely weigh the leaves from all 200 samples, and the corresponding weight data was systematically recorded.

#### 2.4 Hyperspectral image correction

Hyperspectral imagery, comprising hundreds of contiguous spectral bands, is inherently susceptible to degradation from environmental conditions (Yue et al., 2024), atmospheric effects (Andrei et al., 2023), and sensor-related errors (Settembre et al., 2025). To mitigate these impacts, a series of radiometric and atmospheric corrections are essential (Black et al., 2024). For instance, a fundamental step entails converting raw digital numbers (DN) to surface reflectance using methods such as the Empirical Line Method (ELM), which can be represented by the linear transformation in Equation 1:

$$\rho = G \times DN + O \tag{1}$$

Where  $\rho$  is the derived surface reflectance, G is the gain coefficient, DN is the raw digital number from the sensor, and O is the offset coefficient.

These correction procedures significantly enhance the data's radiometric accuracy and spectral fidelity, thereby establishing a reliable foundation for subsequent quantitative analysis and image processing (Gila et al., 2024).

#### 2.5 ROI extraction of hyperspectral image

The ROI (Region of Interest) tool in ENVI 5.3 was used to extract the target regions from the hyperspectral canopy images of Ginkgo biloba, thereby obtaining the ROP sets. By using the average value method to aggregate the spectral data of the target area, a high-quality data set representing the spectral characteristics of ginkgo canopy was constructed. This method effectively eliminates the interference of background noise and abnormal pixels, significantly improves the reliability and representativeness of the data, and lays a solid data foundation for subsequent spectral feature analysis and model construction (Wang X, et al., 2024).

#### 2.6 Hyperspectral data preprocessing

Hyperspectral images are often influenced by environmental and instrumental factors such as temperature, humidity, light intensity, and illumination angle, which can introduce noise into the data. To improve data quality, a series of preprocessing steps were applied, including Multiplicative Scatter Correction (MSC) (Xu et al., 2024), Savitzky–Golay smoothing (SG) (Bing et al., 2018), Standard Normal Variate (SNV) (Jong et al., 2024), First Derivative (FD) (Xunlan et al., 2023), and Standard Scaling (SS) (Faehn et al., 2024).

## 2.7 Construction method of spectral vegetation index

Among the alternative spectral indices, those with a high correlation to ginkgo leaves and a weak intercorrelation were selected. Based on the spectral indices used in relevant references, seven commonly used spectral indices are chosen as alternative indices, and their respective calculation formulas are shown in Table 1. The Normalized Difference Vegetation Index (NDVI), obtained by the ratio of the near-infrared to the red band, reflects the vegetation coverage and Leaf Area Index (LAI), and is often used to assess the health status and biomass of vegetation (Wang et al., 2024). The Red Edge Chlorophyll Index (ReCI), taking advantage of the sensitivity of the red edge band to chlorophyll content, directly reflects the chlorophyll concentration in leaves (Xueyu et al., 2021). The NDRE, calculated as the ratio of the near-infrared to the red edge band, is more sensitive to changes in chlorophyll content, especially in the later stages of vegetation growth. The Green Normalized Difference Vegetation Index (GNDVI), which replaces the red band with the green band, is more sensitive to changes in chlorophyll content (Ge et al., 2019). The SAVI, by introducing a soil adjustment factor, reduces the influence of the soil background on the vegetation index and more accurately reflects the vegetation coverage (Tooley et al., 2024). The SIPI is insensitive to changes in leaf structure and mainly reflects the ratio of carotenoids to chlorophyll (Srivastava et al., 2020). The MSAVI further optimizes the impact of the soil background and is applicable to areas with low vegetation coverage (Shezhou et al., 2015). These seven spectral indices have a high correlation in the prediction of ginkgo leaf yield and a relatively weak correlation with each other. By covering key factors such as leaf area and chlorophyll content, they can effectively evaluate the health status, photosynthetic efficiency, and biomass of ginkgo leaves, providing a scientific basis for yield prediction.

#### 2.8 Characteristic band screening

To effectively reduce the complexity and redundancy of hyperspectral data, this study employs feature band selection methods to enhance data processing efficiency and improve the accuracy and reliability of yield prediction models by identifying key bands most relevant to ginkgo leaf yield. The hyperspectral dataset was first divided into training, validation, and test sets in a 70%:15%:15% ratio to ensure the independence of model evaluation. Subsequently, feature band selection was performed using Particle Swarm Optimization (PSO) (Wei et al., 2024), Successive Projections Algorithm (SPA) (Souza et al., 2025), Principal Component Analysis (PCA) (Matinfar et al., 2025), Least Absolute Shrinkage and Selection Operator (LASSO) ( (Stevens et al., 2025), Competitive Adaptive Reweighted Sampling (CARS) (Shi et al., 2024), Spectral Index (SI) (Wang et al., 2024), and the Particle Swarm Attention Mechanism Algorithm (PSAMA). The working principles of all algorithms will be systematically elaborated below, with particular emphasis on PSO and its improved version, PSAMA.

The core idea of PSO is to explore and find the optimal solution by simulating a group of particles in the search space. Each particle represents a possible solution. Through 'flying' in the search space, the particle swarm gradually adjusts its position by using its own historical experience and group collaboration information, and finally converges to the global optimal solution (Ren et al., 2024), as shown in Equations 2 and 3.

$$v_{i}^{d} = w * v_{i}^{d-1} + c_{1} * r_{1} * \left(pbest_{i}^{d} - x_{i}^{d}\right) + c_{2} * r_{2} * \left(gbest_{i}^{d} - x_{i}^{d}\right) \tag{2}$$

$$x_i^{d+1} = x_i^d + v_i^d (3)$$

Where  $c_1$  is individual learning factor,  $c_2$  social learning factor, w velocity inertia weight,  $v_i^d$  the speed of the d th iteration of the i th particle,  $x_i^d$  the position of the d th iteration of the i th particle, pb  $est_i^d$  the i th particle iterates to the best position of the d th iteration,  $gbest_i^d$  all particles iterate to the best position by d times.

PSAMA mainly introduces the Attention Mechanism into the PSO algorithm, which dynamically adjusts the attention degree of information by adjusting the position of particles. The core idea is to calculate the weight coefficient of each key 's corresponding value (Value) according to the correlation between Query and Key, and then obtain the final output by weighted summation, that is, the final Attention values. In essence, the Attention mechanism is the weighted summation of the Value values of the elements in the Source, and Query and Key are used to calculate the weight

TABLE 1 Operation formula of spectral vegetation index.

Spectral Index	Computing Formula
NDVI	$(NIR_{801} - RED_{682})/(NIR_{801} + RED_{682})$
ReCI	(NIR <sub>801</sub> /RED <sub>701</sub> ) -1
NDRE	$(NIR_{801} - RED EDGE_{720})/(NIR_{801} + RED EDGE_{720})$
GNDVI	(NIR <sub>801</sub> - GREEN <sub>561</sub> )/(NIR <sub>801</sub> + GREEN <sub>561</sub> )
SAVI	$((NIR_{820} - RED_{680})/(NIR_{820} + RED_{680} + L)) * (1 + L)$
SIPI	(NIR <sub>820</sub> – BLUE <sub>462</sub> )/(NIR <sub>820</sub> – RED <sub>712</sub> )
MSAVI	$0.5[(2{\rm NIR_{801}}+1-{\rm SQRT}((2{\rm NIR_{801}}+1)^2-8~({\rm NIR_{801}}-{\rm RED_{682}}))]$

Where because ginkgo biloba belongs to the low green vegetation area, L=1.

TABLE 2 Comparative analysis of different pretreatment methods and the original spectral PLSR model.

Different regression	Pretreatment method	Calibration set		Prediction set	
models		$R_C^2$	RMSE <sub>c</sub>	$R_P^2$	RMSE <sub>p</sub>
PLSR	Original	0.9217	0.0312	0.7658	0.0218
	MSC	0.9345	0.0217	0.7532	0.0445
	SNV	0.9624	0.0232	0.7831	0.0325
	SG	0.9021	0.0147	0.6957	0.0544
	FD	0.8912	0.0322	0.6621	0.0467
	SS	0.8845	0.0455	0.6327	0.0171

coefficient of the corresponding value (Lang et al., 2024). Its working principle is shown in Figure 3 and Equation 4.

According to the principle of attention mechanism, the calculation formula is as follows:

$$Attention(Query, Source) = \sum_{i=1}^{L_x} Similarity(Query, Key_i) * Value_i \ (4)$$

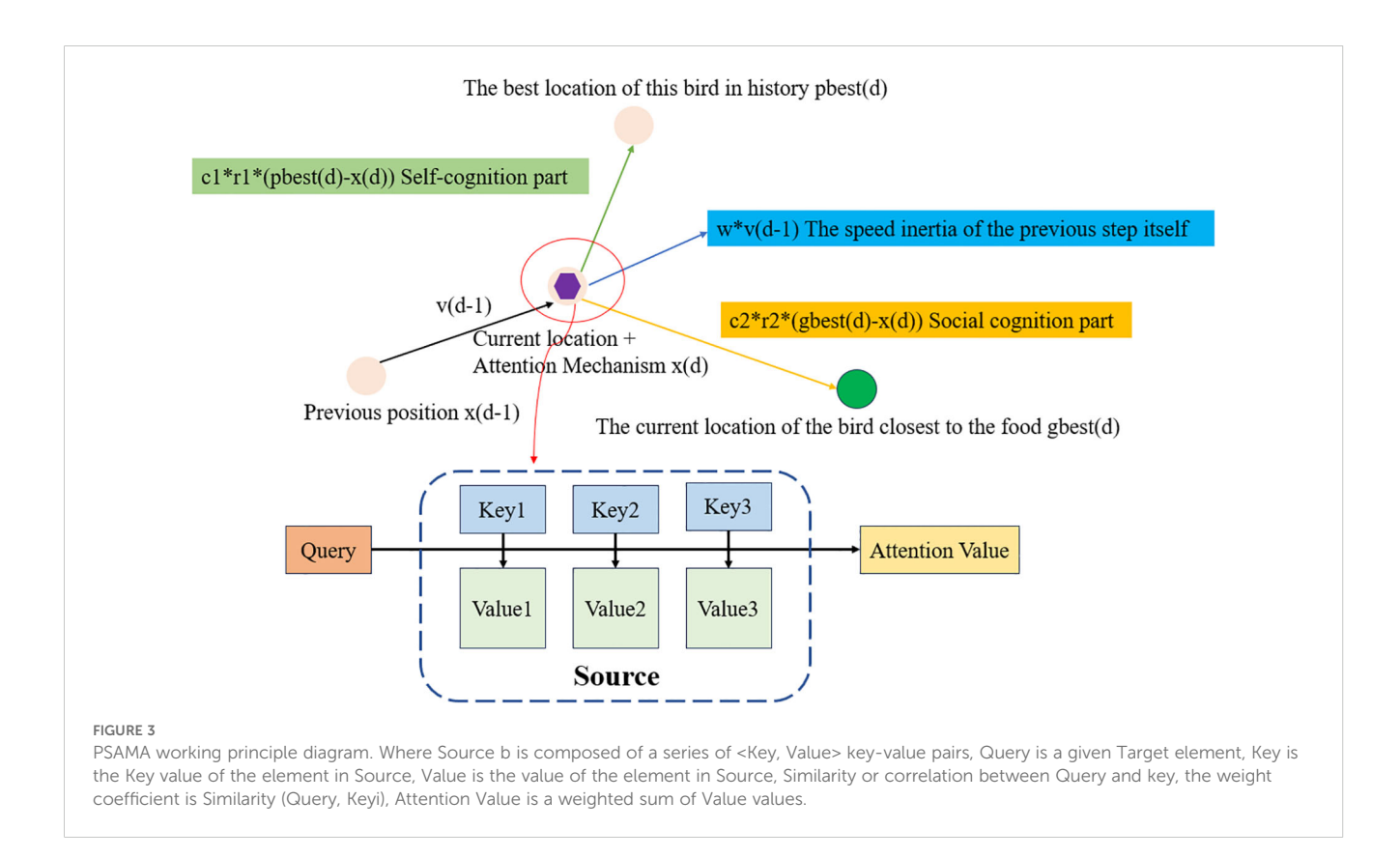
Where  $L_x = || Source ||$  denotes the length of Source.

#### 2.9 Machine learning and model validation

The optimal model was selected from seven machine learning regression methods, all employing Grid Search Cross-Validation (GridSearchCV) for hyperparameter optimization. The methods and their respective tuned hyperparameters include: PLSR (Sun et al., 2024) with n\_components; RF (Sun et al., 2024) with n\_estimators; KNNR (Song et al., 2025) with n\_neighbors; LSTM (Satyabrata et al., 2024) with learning rate; SVR (Tian et al., 2025)

TABLE 3 Feature bands selected by different algorithms.

Algorithm of feature band screening	Filtered bands/nm	Number of bands
Particle Swarm Optimization (PSO)	408,438,446,535,685,691,701, 728,892,951	10
Particle Swarm Attention Mechanism Algorithm (PSAMA)	440,446,473,491,545,551,645,666,672,704,723, 734,766,800,884,925,930,962,970,989	20
Successive Projections Algorithm (SPA)	400,403,680,730,760,920,930,950,980,1000	10
Principal Component Analysis (PCA)	400,403,406,408,409,411,413,416,419,421,424,426,429,432,434,437,440,442,445,448,450	21
Least Absolute Shrinkage and Selection Operator (LASSO)	408,411,424,432,440,446,456,462,465,470,473,491,500,766,906,933,946,957,970,973	20
Competitive Adaptive Reweighted Sampling (CARS)	408,416,422,443,454,470,473,481,502,540,607,610,736,739,900,903,906,914,916,919,922,925,956	23



with regularization parameter C; BiLSTM (Sun X, et al., 2024) with learning rate; and BiLSTM-GS, which simultaneously optimizes both learning rate and hidden layer sizes.

The BiLSTM-GS model integrates the BiLSTM architecture with the GridSearchCV algorithm (Liang et al., 2024). While the standard BiLSTM model only tunes the learning rate, BiLSTM-GS introduces an additional hyperparameter—hidden layer size—to achieve more comprehensive optimization. As an enhanced LSTM variant, BiLSTM processes sequences bidirectionally (forward and backward), enabling more effective capture of contextual dependencies (Zhang et al., 2025). GridSearchCV automates hyperparameter selection through systematic cross-validation, significantly improving model performance. The architecture of the BiLSTM-GS model is illustrated in Figure 4.

Building upon the bidirectional processing capability of BiLSTM, this study leverages its strength in modeling the continuous spectral-temporal sequences of ginkgo leaves. The network architecture enables integrated learning of both forward and backward dependencies within the spectral data, effectively capturing the cumulative physiological changes during leaf growth. This approach significantly enhances the characterization of long-term developmental trends, thereby improving the robustness of yield prediction.

During model configuration, particular attention was given to the interaction between hidden layer dimensionality and learning rate (Nikzad et al., 2025). The hidden layer structure governs the model's capacity to represent complex spectral patterns, while the learning rate regulates the convergence behavior during training. Proper coordination between these two parameters ensures stable gradient propagation while preventing either underfitting due to insufficient model expressivity or overfitting caused by excessive parameterization, ultimately leading to optimized generalization performance (Wan et al., 2024).

The determination coefficient  $R^2$  and the root mean square error RMSE are used as the evaluation indexes of the regression model. The larger the  $R^2$  of the model, the smaller the RMSE, and the better the training effect of the model (Long et al., 2024), where  $R_c^2$ ,  $RMSE_c$  is the results of the training set, and  $R_p^2$ ,  $RMSE_p$  is the results of the calibration set. The calculation formulas are shown in Equations 5 and 6.

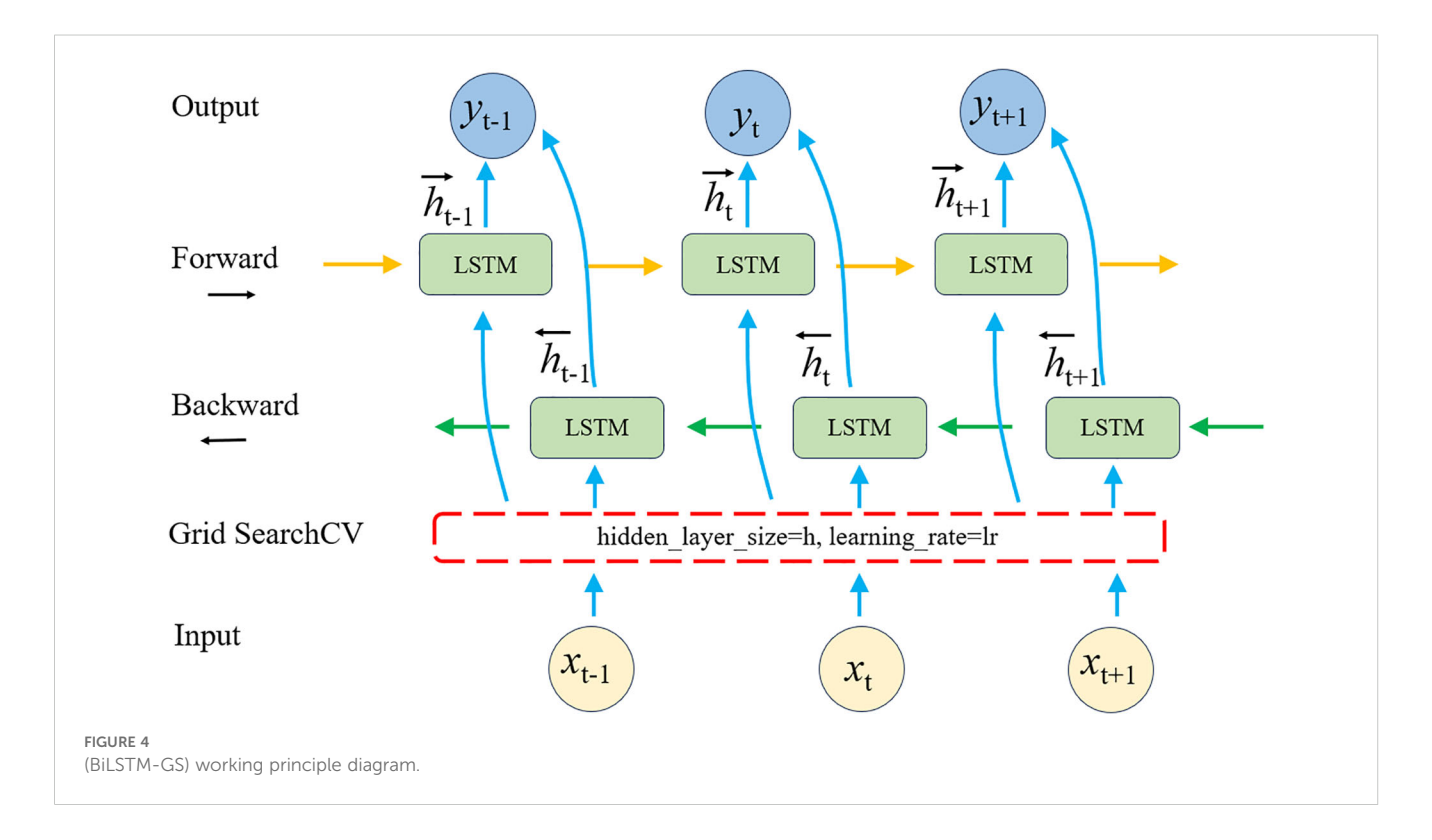
$$R^{2} = 1 - \frac{\sum_{i=1}^{N} (y_{i} - \widehat{y}_{i})^{2}}{\sum_{i=1}^{N} (y_{i} - \overline{y})^{2}}$$
 (5)

$$RMSE = \sqrt{\frac{1}{N} \sum_{i=1}^{N} (y_i - \hat{y_i})^2}$$
 (6)

Where N is the number of samples,  $y_i$  is the actual value of the ith sample,  $\hat{y}_i$  is the actual value of the ith sample, and  $\bar{y}$  is the actual mean value of all samples.

### 2.10 Experimental platform and computing environment

All experiments were conducted on a workstation equipped with an Intel Core i7-12700H CPU and 32 GB of RAM. The entire training and hyperparameter tuning process for all models was



performed on this CPU platform without GPU acceleration. The software environment utilized PyCharm 2023.2.4 (Community Edition) with Python 3.9, incorporating key libraries such as PyTorch (1.8), scikit-learn (1.2.2), and TensorFlow (2.10.0). The complete workflow required approximately 10 minutes on the specified hardware, demonstrating the computational efficiency of the proposed methodology on standard computing resources.

#### 3 Results and discussion

#### 3.1 Spectral pretreatment

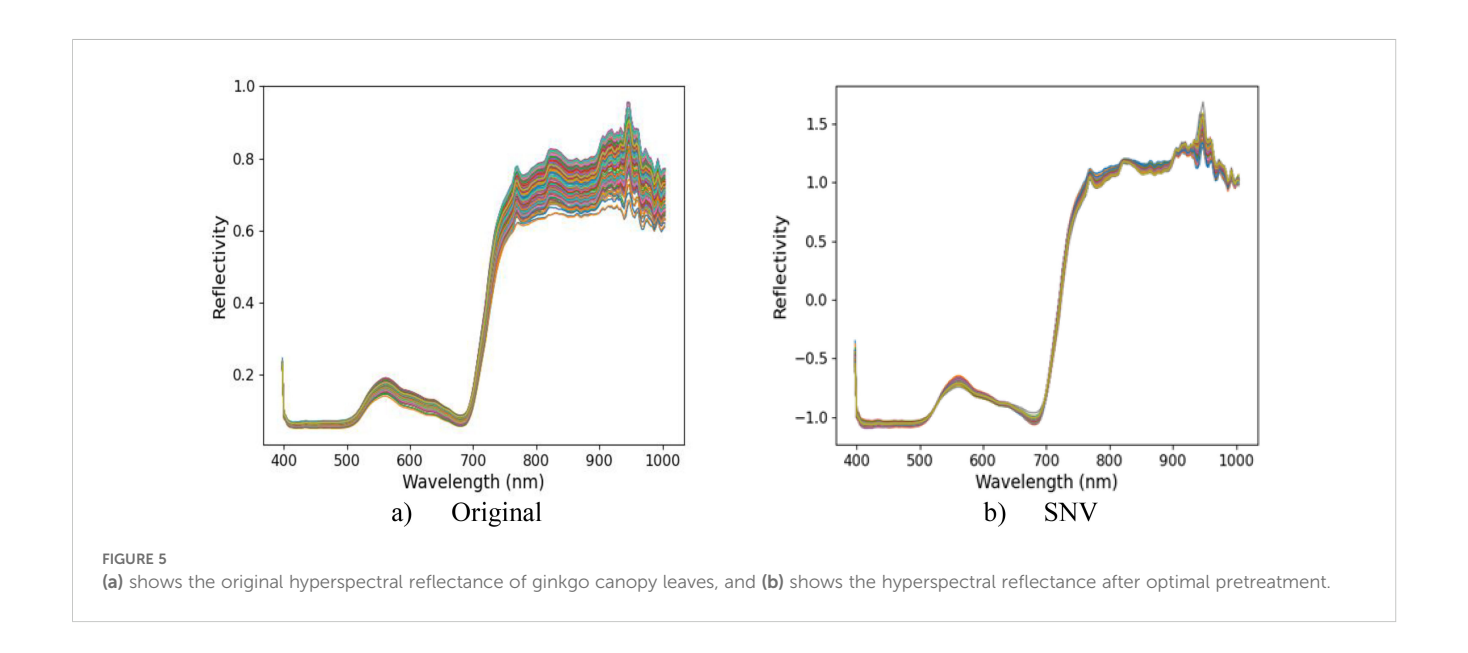
Five spectral data preprocessing methods (MSC, SNV, SG, FD, and SS) and PLSR were used to establish regression models for leaf yield of different Ginkgo trees. The prediction results of each model are shown in Table 2. The  $R_6^2$  and  $R_P^2$  of different models were higher than the original spectrum, which can be used to detect the yield of ginkgo leaves. Among these models, the SNV model exhibited the highest accuracy with  $R_P^2 = 0.7831$  and  $RMSE_p = 0.0325$ . Therefore, the SNV pretreatment model was used as the basis for subsequent data processing. The hyperspectral original reflectance and the best pretreatment reflectance are shown in Figure 5. The weak absorption peak near 820 nm was related to the stretching vibration of the N-H triplet state (Chitra et al., 2022). A smaller absorption peak appears near 930 nm, mainly due to the dualfrequency absorption of O-H (Chitra et al., 2022). The peaks and troughs near 560 nm and 690 nm were caused by chlorophyll and carotenoids at ginkgo leaves (Marchese et al., 2024). These spectral characteristics further confirmed the intrinsic relationship between the chemical composition of Ginkgo biloba leaves and their spectral information, providing strong support for further understanding the spectral characteristics of Ginkgo biloba leaves.

#### 3.2 Spectral vegetation index selection

In this study, the random forest stepwise regression method was used to select the vegetation index with less redundant information between each other to construct the vegetation index combination for ginkgo leaf yield estimation. Figure 6a is the ranking of the importance of 7 vegetation index features. It can be seen from the graph that the ReCI vegetation index exhibited the highest importance of 0.3367, followed by the NDVI vegetation index, and the vegetation index with the smallest feature importance is GNDVI. Figure 6b depicts five main vegetation indices selected by random forest stepwise regression method, which are ReCI, NDVI, GNDVI, SAVI and MSAI.

The correlation analysis results of Figure 7 show that GNDVI and NDRE were highly positively correlated (r=0.93), indicating that they have similar spectral response characteristics and can be used interchangeably to reduce data redundancy. However, GNDVI and SIPI (r=-0.90), SAVI and MSAVI (r=-0.98), and SIPI and NDRE (r=-0.99) showed significant negative correlations. These index combinations may represent different vegetation physiological characteristics or environmental stress responses. Therefore, SAVI, MSAVI, NDRE and SIPI were finally selected as the representative vegetation index combination, which can not only fully reflect the vegetation status, but also effectively avoid information redundancy.

Based on the above analysis, the spectral indices suitable for model input include SAVI, MSAVI, NDRE and SIPI. The



combination of these indices has low redundancy information, which can effectively reflect the characteristic information of vegetation from multiple dimensions, and provides a more comprehensive and accurate input variable for the estimation of ginkgo leaf yield.

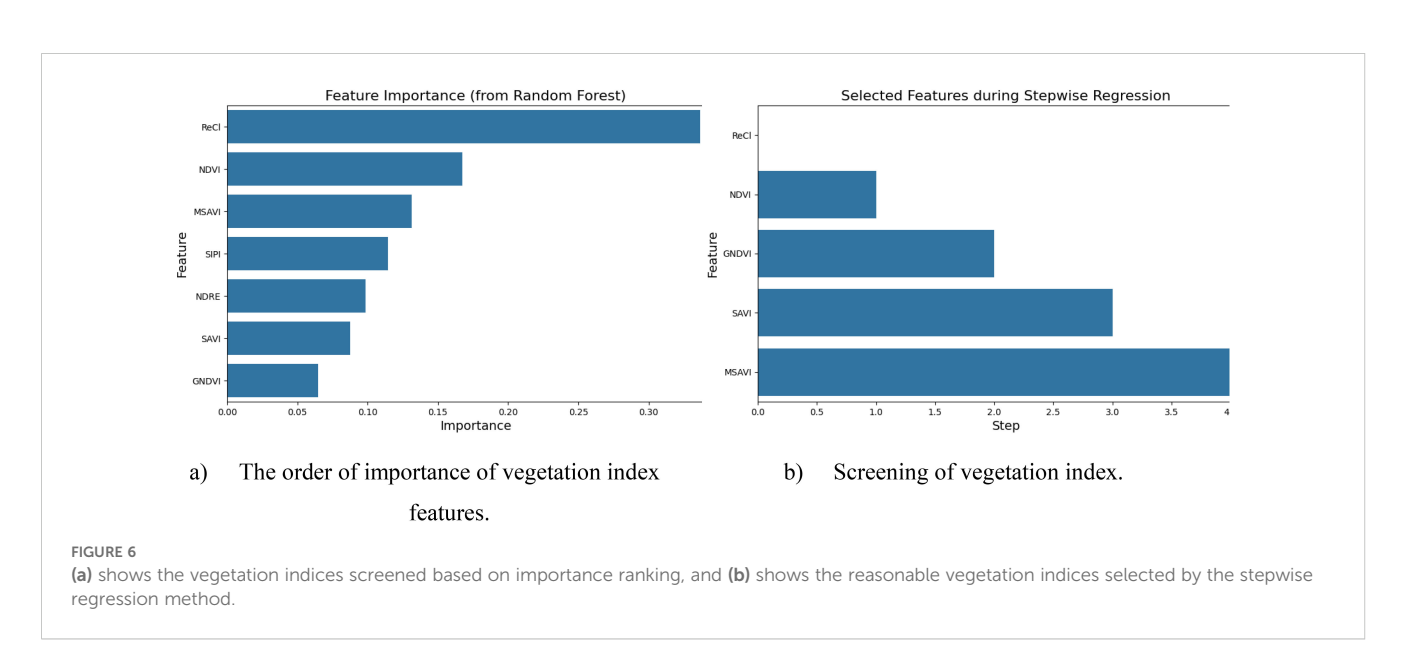
#### 3.3 Feature band extraction

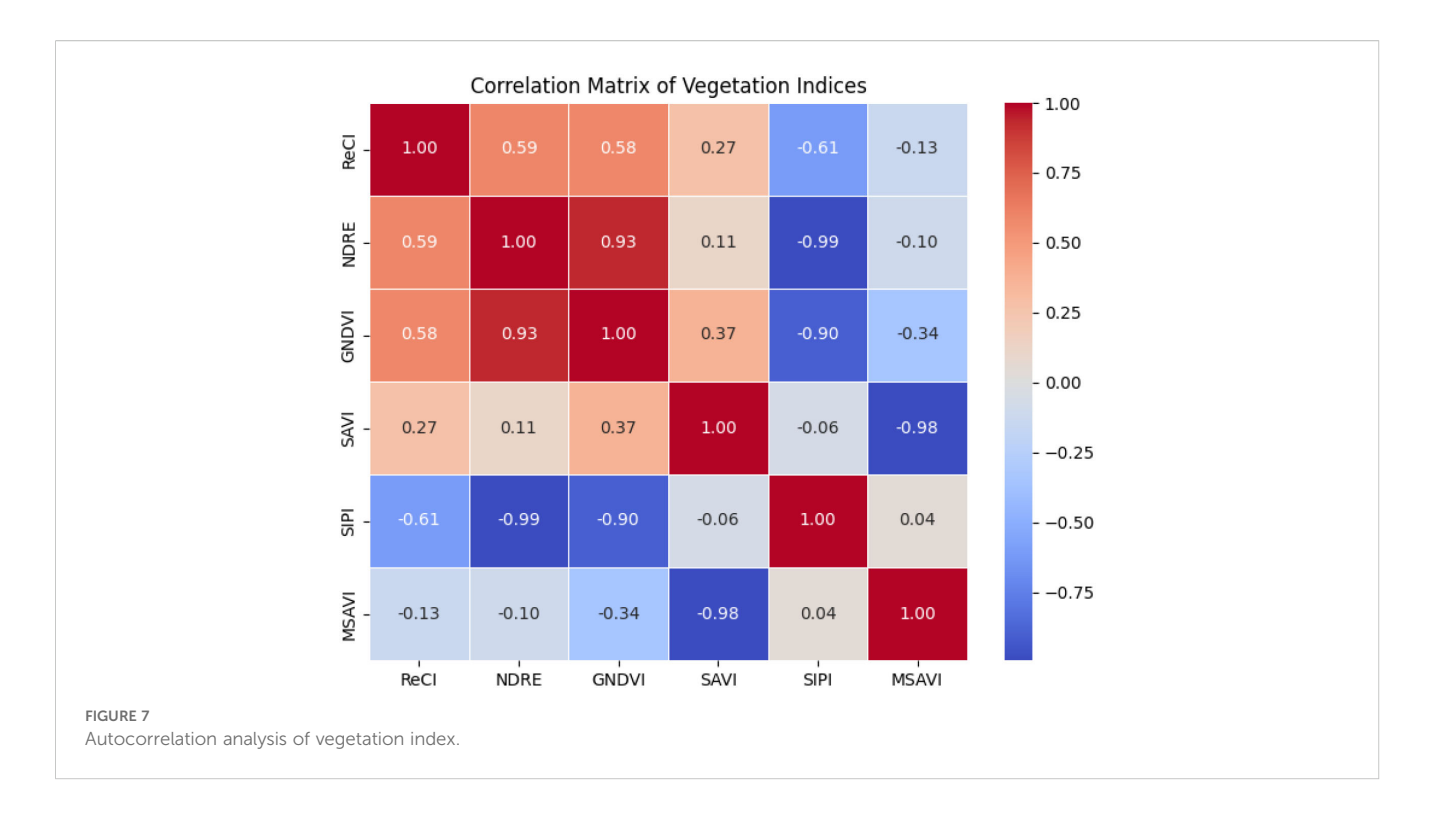
In this study, a variety of feature band screening methods were used to analyze the spectral data preprocessed by SNV. Among them PSO, SPA, PSAMA, LASSO and CARS were used to filter the characteristic bands (10,10,20,20 and 23, respectively), which were evenly distributed in the range of 400  $\sim$  1000 nm, effectively reducing redundant information and retaining the most representative spectral features. In contrast, the 21 characteristic

bands screened by PCA were mainly concentrated in the short-wave region of  $400 \sim 450$  nm, showing unique wavelength selection characteristics. The results are shown in Table 3. Different feature selection methods have both commonalities in band distribution (most methods select wide spectral range features) and their own characteristics (PCA focusing on shortwave regions), which provides a variety of feature selection schemes for subsequent spectral analysis.

## 3.4 Prediction results using different machine learning and feature band screening methods

This study utilized full-band spectra, vegetation indices, and feature-selected spectral bands as input variables for a suite of





machine learning and deep learning models. Specifically, A1 represents the complete set of 224 bands, while A2 to A8 correspond to features selected by vegetation indices, Particle Swarm Optimization (PSO), PSO with an attention mechanism, Successive Projections Algorithm (SPA), Principal Component Analysis (PCA), Least Absolute Shrinkage and Selection Operator (LASSO), and Competitive Adaptive Reweighted Sampling (CARS), respectively. To enhance estimation accuracy, A2 (spectral indices) and the Region of Interest Pixel set (denoted as B) were systematically combined with A1 and the bands from A3 to A8. Through systematic pairing with models including PLSR, RF, KNNR, LSTM, SVR, BiLSTM, and BiLSTM-GS, a total of 168 distinct data-model combinations were generated. All model hyperparameters were optimized via grid search cross-validation, with the final configurations established as follows: PLSR (n\_components=10), RF (n\_estimators=200), KNNR (n\_neighbors=10), SVR (C = 10), LSTM (learning\_rate=0.01), BiLSTM (learning\_rate=0.01), and BiLSTM-GS (learning\_rate=0.01, hidden\_layer\_sizes=50).

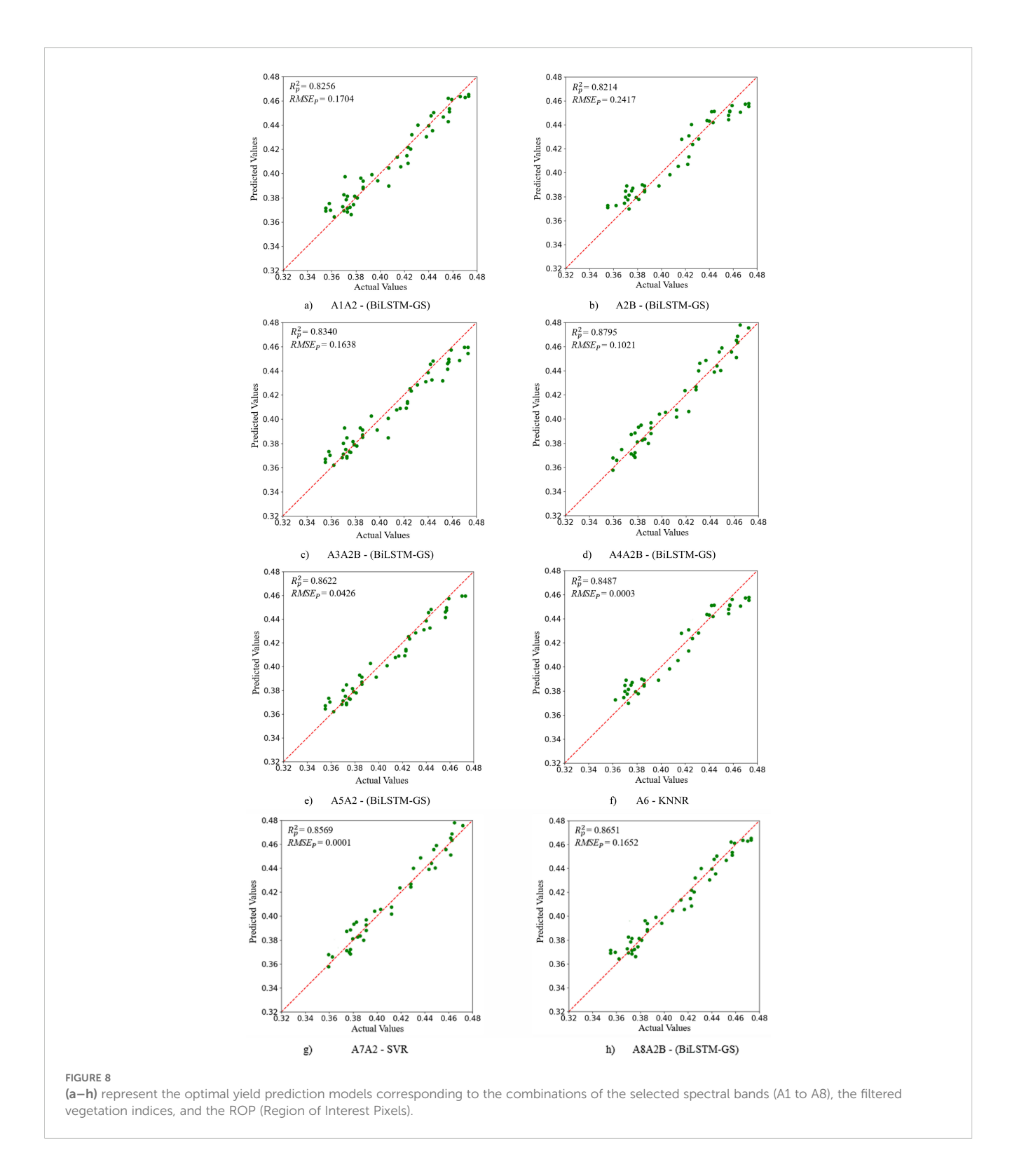
As shown in Table 4, when A4A2B was used as the input variable, the BiLSTM-GS model achieved the highest prediction accuracy ( $R_p^2 = 0.8795$ ,  $RMSE_p = 0.1021$ ). To visually illustrate the optimal prediction yield models corresponding to the combination of A1  $\sim$  A8 bands and spectral vegetation indices, eight regression diagrams were used, as shown in Figure 8.

To obtain the best accuracy of the model (BiLSTM-GS), the grid SearchCV algorithm was used to optimize the hyper-parameters of the BiLSTM model, and the hyper-parameter learning rate and the size of the hidden layer was used as input. The (BiLSTM-GS) model determination coefficient ( $R_P^2$ ) is the output to draw the heat map. The results are shown in Figure 9. The deeper the red color, the higher the determination coefficient ( $R_P^2$ ) corresponding to the

(BiLSTM-GS) model, and the better the fitting performance. When the (BiLSTM-GS) model obtained the best  $R_P^2 = 0$ . 8795, the corresponding optimal learning rate and hidden layer size were 0.01 and 50, respectively.

#### 3.5 Model generalization ability validation

To validate the model's generalization performance, an external public dataset, LOPEX1993, was employed. LOPEX1993 is an open spectral data set focusing on vegetation research, with rich spectral information of vegetation. In this study, PLSR, RF, KNNR, SVR, BiLSTM and BiLSTM-GS were used to detect the chemical component content of the data set. Table 5 shows that the (BiLSTM-GS) model achieved the highest detection accuracy. Through the above comparative analysis, it can be found that BiLSTM has the following advantages over models such as PLSR, RF, KNNR and SVR. First, as the only model that can capture sequence context information in both directions, BiLSTM does not need to rely on manual design features (such as RF requires feature engineering, KNNR needs to define distance metrics). Second, its unique forgetting gate, input gate and output gate mechanism can dynamically adjust the information flow and effectively solve the long-term dependence problem (better than PLSR). In addition, in sequence data tasks such as natural language processing, BiLSTM performs significantly better than traditional methods (such as SVR). The hyperparameters optimized by Grid SearchCV further improve the performance of the model, so that the trained model can achieve higher prediction accuracy. Therefore, the prediction effect of the (BiLSTM-GS) model on the LOPEX1993 public dataset is significantly better than other comparison models.



#### 3.6 Discussion

This study systematically developed and validated a hyperspectral inversion model for ginkgo leaf yield prediction by integrating advanced preprocessing, feature selection, and machine learning techniques. The optimal SNV- (SAVI - MSAVI – NDRE - SIPI - ROP) - (BiLSTM-GS) model achieved superior performance

 $(R_P^2 = 0.8795)$ , demonstrating the significant potential of airborne hyperspectral imaging for non-destructive yield assessment in economic forestry.

Our findings reveal that SNV preprocessing yielded optimal PLSR performance ( $R_P^2 = 0.7831$ ), aligning with regarding its robustness in mitigating scattering effects (Jin et al., 2023). The proposed PSAMA algorithm effectively identified 20 key bands

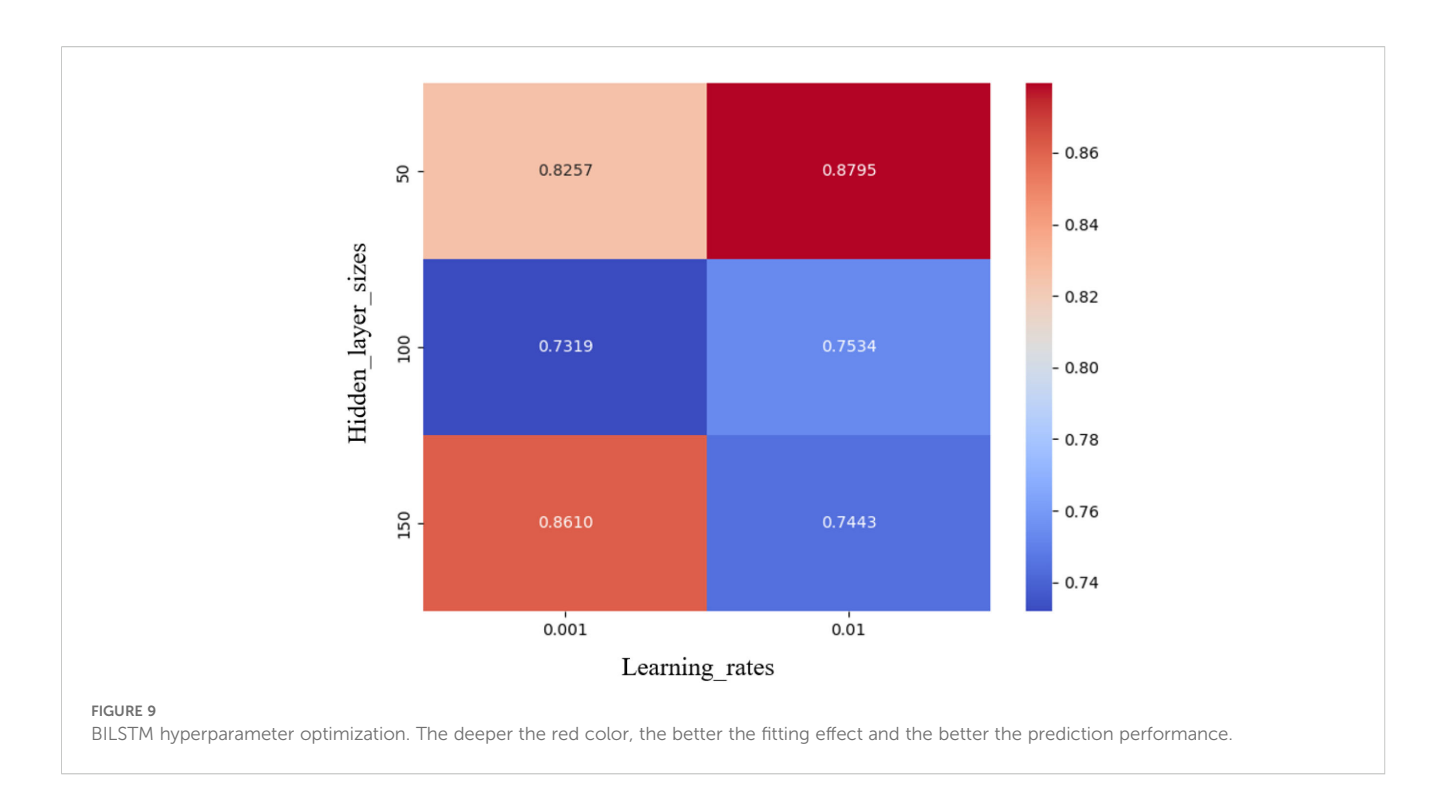


TABLE 4 Ginkgo biloba leaf chlorophyll content prediction model results.

Input variable	Modeling method	$R_C^2$	$RMSE_c$	$R_P^2$	RMSE <sub>p</sub>
	PLSR	0.9324	0.0221	0.7831	0.0318
	RF	0.9421	0.0181	0.7902	0.0221
A1	KNNR	0.8234	0.0003	0.6911	0.0005
	LSTM	0.2443	0.0012	0.1846	0.0011
	SVR	0.9669	0.0001	0.8053	0.0001
	BiLSTM	0.8824	0.0112	0.7621	0.0332
	(BiLSTM-GS)	0.9354	0.0181	0.7541	0.0423
	PLSR	0.9256	0.0021	0.7654	0.0211
A1B	RF	0.9624	0.0079	0.6652	0.0213
	KNNR	0.8121	0.0003	0.6832	0.0005
	LSTM	0.2425	0.0013	0.1845	0.0011
	SVR	0.9534	0.0001	0.7821	0.0001
	BiLSTM	0.9345	0.1071	0.7956	0.1456
	(BiLSTM-GS)	0.9324	0.1545	0.7733	0.1517
	PLSR	0.9347	0.0079	0.7315	0.0119
	RF	0.9417	0.0077	0.6012	0.2181
4142	KNNR	0.8323	0.0003	0.7012	0.0005
A1A2	LSTM	0.3356	0.0012	0.2956	0.0016
	SVR	0.9521	0.0001	0.6984	0.0001
	BiLSTM	0.9447	0.1145	0.7322	0.1458

TABLE 4 Continued

Input variable	Modeling method	$R_C^2$	$RMSE_c$	$R_P^2$	$RMSE_p$
	(BiLSTM-GS)	0.9347	0.1046	0.8256	0.1704
	PLSR	0.9627	0.0078	0.7258	0.0124
	RF	0.9356	0.0076	0.6145	0.0256
	KNNR	0.8458	0.0003	0.7815	0.0005
A1A2B	LSTM	0.3357	0.0012	0.2856	0.0016
	SVR	0.9625	0.0001	0.6856	0.0001
	BiLSTM	0.9432	0.1025	0.7232	0.0225
	(BiLSTM-GS)	0.9458	0.1033	0.7811	0.1625
	PLSR	0.9021	0.0201	0.4350	0.0282
	RF	0.9570	0.0080	0.6287	0.0231
	KNNR	0.8325	0.0003	0.7625	0.0005
A2	LSTM	0.3343	0.0012	0.2928	0.0016
	SVR	0.9322	0.0001	0.6654	0.0001
	BiLSTM	0.9174	0.0256	0.7200	0.3561
	(BiLSTM-GS)	0.9344	0.3838	0.7902	0.3579
	PLSR	0.9334	0.0168	0.6678	0.0045
	RF	0.9541	0.0276	0.7215	0.0258
	KNNR	0.8856	0.0003	0.7659	0.0005
A2B	LSTM	0.3459	0.0012	0.2859	0.0016
	SVR	0.9542	0.0001	0.6854	0.0001
	BiLSTM	0.9324	0.0217	0.7542	0.0215
	(BiLSTM-GS)	0.9657	0.025	0.8214	0.2417
	PLSR	0.8855	0.0140	0.7921	0.0212
	RF	0.9051	0.0278	0.6453	0.0576
	KNNR	0.8845	0.0003	0.7589	0.0005
A3	LSTM	0.3357	0.0012	0.2757	0.0016
	SVR	0.9534	0.0001	0.6751	0.0001
	BiLSTM	0.8845	0.0384	0.7014	0.0332
	(BiLSTM-GS)	0.9533	0.0257	0.7845	0.0323
	PLSR	0.9425	0.0317	0.6954	0.0325
	RF	0.9514	0.0068	0.6957	0.0151
	KNNR	0.8824	0.0003	0.7589	0.0005
A3B	LSTM	0.3468	0.0012	0.2958	0.0016
	SVR	0.9457	0.0001	0.6578	0.0001
	BiLSTM	0.9633	0.1122	0.7832	0.0189
	(BiLSTM-GS)	0.9422	0.0256	0.7789	0.1659
	PLSR	0.8327	0.0334	0.6241	0.0229
A3A2	RF	0.9499	0.0086	0.5064	0.0267
	RF	0.9499	0.0086	0.5064	0.0267

TABLE 4 Continued

Input variable	Modeling method	$R_C^2$	$RMSE_c$	$R_P^2$	$RMSE_p$
	KNNR	0.8853	0.0003	0.7128	0.0005
	LSTM	0.3365	0.0012	0.2845	0.0016
	SVR	0.9247	0.0001	0.6941	0.0001
	BiLSTM	0.9212	0.1165	0.7602	0.2146
	(BiLSTM-GS)	0.8656	0.1544	0.7659	0.2142
	PLSR	0.8485	0.0225	0.5921	0.0265
	RF	0.9321	0.0078	0.6214	0.0325
	KNNR	0.8826	0.0003	0.7133	0.0005
A3A2B	LSTM	0.3345	0.0012	0.2625	0.0016
	SVR	0.9326	0.0001	0.7556	0.0001
	BiLSTM	0.9215	0.1026	0.7626	0.2021
	(BiLSTM-GS)	0.8854	0.1577	0.8340	0.1638
	PLSR	0.8911	0.3154	0.7751	0.4273
	RF	0.9355	0.0102	0.6972	0.0206
	KNNR	0.8832	0.0003	0.7142	0.0005
A4	LSTM	0.3256	0.0012	0.2524	0.0016
	SVR	0.9235	0.0001	0.7332	0.0001
	BiLSTM	0.8933	0.0246	0.7712	0.0421
	(BiLSTM-GS)	0.9512	0.0117	0.7969	0.0235
	PLSR	0.8824	0.0217	0.6325	0.0256
	RF	0.9145	0.0088	0.6954	0.0227
	KNNR	0.8825	0.0003	0.7132	0.0005
A4B	LSTM	0.3326	0.0012	0.2845	0.0016
	SVR	0.9247	0.0001	0.7569	0.0001
	BiLSTM	0.9215	0.1031	0.8254	0.0332
	(BiLSTM-GS)	0.9256	0.0795	0.8341	0.1897
	PLSR	0.8541	0.0217	0.6874	0.0213
	RF	0.9321	0.0121	0.6789	0.0258
	KNNR	0.8844	0.0003	0.7245	0.0005
A4A2	LSTM	0.3318	0.0012	0.2832	0.0016
	SVR	0.9312	0.0001	0.7421	0.0001
	BiLSTM	0.9328	0.0545	0.7427	0.1032
	(BiLSTM-GS)	0.9425	0.0617	0.8021	0.0856
	PLSR	0.8625	0.0218	0.6562	0.0217
	RF	0.9256	0.0129	0.6654	0.0235
A4A2B	KNNR	0.8838	0.0003	0.7238	0.0005
	LSTM	0.3412	0.0012	0.2858	0.0016
	SVR	0.9314	0.0001	0.7325	0.0001

TABLE 4 Continued

Input variable	Modeling method	$R_C^2$	RMSE <sub>c</sub>	$R_P^2$	RMSE <sub>p</sub>
	BiLSTM	0.9456	0.0325	0.7328	0.0256
	(BiLSTM-GS)	0.9422	0.0817	0.8795	0.1021
	PLSR	0.9324	0.0221	0.7831	0.0318
	RF	0.9421	0.0181	0.7902	0.0221
	KNNR	0.8603	0.0002	0.7436	0.0004
	LSTM	0.3418	0.0012	0.2842	0.0016
A5	SVR	0.9315	0.0001	0.7412	0.0001
	BiLSTM	0.8824	0.0112	0.7621	0.0332
	(BiLSTM-GS)	0.9354	0.0181	0.7541	0.0423
	PLSR	0.9324	0.0115	0.7624	0.0312
	RF	0.9425	0.0141	0.7617	0.0125
	KNNR	0.8633	0.0017	0.7512	0.0021
A5B	LSTM	0.2754	0.0158	0.2944	0.0451
	SVR	0.9321	0.0001	0.7418	0.0001
	BiLSTM	0.9345	0.0121	0.7578	0.0158
	(BiLSTM-GS)	0.9358	0.0178	0.8208	0.0224
	PLSR	0.9524	0.0325	0.7415	0.0135
	RF	0.9316	0.0124	0.7352	0.0164
	KNNR	0.8066	0.0003	0.7021	0.0005
A5A2	LSTM	0.3021	0.0012	0.2854	0.0010
	SVR	0.9326	0.0001	0.7215	0.0001
	BiLSTM	0.9433	0.0154	0.7435	0.0158
	(BiLSTM-GS)	0.9447	0.0125	0.8622	0.0426
	PLSR	0.9625	0.0244	0.7423	0.0323
	RF	0.9416	0.0132	0.7456	0.0118
	KNNR	0.8356	0.0003	0.6868	0.0005
A5A2B	LSTM	0.3029	0.0012	0.2824	0.0010
	SVR	0.9521	0.0001	0.7524	0.0001
	BiLSTM	0.9332	0.0156	0.7318	0.0118
	(BiLSTM-GS)	0.9254	0.0135	0.8327	0.0565
	PLSR	0.9324	0.0221	0.7831	0.0318
	RF	0.9421	0.0181	0.7902	0.0221
	KNNR	0.9276	0.0001	0.8487	0.0003
A6	LSTM	0.0287	0.0016	0.0192	0.0014
	SVR	0.9524	0.0001	0.7621	0.0001
	BiLSTM	0.8824	0.0112	0.7621	0.0332
	(BiLSTM-GS)	0.9354	0.0181	0.7541	0.0423
A6B	PLSR	0.9526	0.0225	0.7354	0.0156

TABLE 4 Continued

A6A2B  A6A2B  I (Bil	RF KNNR LSTM SVR BiLSTM LSTM-GS) PLSR RF KNNR LSTM SVR BiLSTM LSTM-GS) PLSR RF KNNR LSTM LSTM-GS) PLSR RF KNNR LSTM-GS)	0.9421 0.9468 0.3716 0.9417 0.8625 0.9521 0.7547 0.9538 0.8094 0.3720 0.9357 0.8818 0.9627 0.7857 0.9524 0.8635 0.3457 0.9356	0.0146 0.0001 0.0011 0.0001 0.0113 0.0145 0.0204 0.0232 0.0003 0.0011 0.0154 0.0134 0.0145 0.0136 0.0003 0.0011	0.7541 0.8145 0.3059 0.7456 0.7754 0.8215 0.7457 0.7459 0.6486 0.3089 0.7425 0.7457 0.8151 0.7326 0.7638 0.6745	0.0236 0.0001 0.0010 0.0001 0.0364 0.0336 0.0115 0.0118 0.0006 0.0010 0.0001 0.0112 0.0325 0.0135 0.0115 0.0006
A6A2  I (Bil	SVR SVR BiLSTM  LSTM-GS)  PLSR  RF  KNNR  LSTM  SVR  BiLSTM  LSTM  SVR  BiLSTM  LSTM-GS)  PLSR  RF  KNNR  LSTM-GS)	0.3716 0.9417 0.8625 0.9521 0.7547 0.9538 0.8094 0.3720 0.9357 0.8818 0.9627 0.7857 0.9524 0.8635 0.3457	0.0011 0.0001 0.0113 0.0145 0.0204 0.0232 0.0003 0.0011 0.00154 0.0134 0.0145 0.0136 0.0003	0.3059 0.7456 0.7754 0.8215 0.7457 0.7459 0.6486 0.3089 0.7425 0.7457 0.8151 0.7326 0.7638	0.0010 0.0001 0.0364 0.0336 0.0115 0.0118 0.0006 0.0010 0.0011 0.0112 0.0325 0.0135 0.0115
A6A2  I (Bil	SVR  BILSTM  LSTM-GS)  PLSR  RF  KNNR  LSTM  SVR  BILSTM  LSTM-GS)  PLSR  RF  KNNR  LSTM-GS)	0.9417  0.8625  0.9521  0.7547  0.9538  0.8094  0.3720  0.9357  0.8818  0.9627  0.7857  0.9524  0.8635  0.3457	0.0001 0.0113 0.0145 0.0204 0.0232 0.0003 0.0011 0.00154 0.0134 0.0145 0.0136 0.0003	0.7456 0.7754 0.8215 0.7457 0.7459 0.6486 0.3089 0.7425 0.7457 0.8151 0.7326 0.7638	0.0001 0.0364 0.0336 0.0115 0.0118 0.0006 0.0010 0.0001 0.0112 0.0325 0.0135 0.0115
A6A2B  A6A2B  I (Bil	BILSTM  LSTM-GS)  PLSR  RF  KNNR  LSTM  SVR  BILSTM  LSTM-GS)  PLSR  RF  KNNR  LSTM-GS)	0.8625 0.9521 0.7547 0.9538 0.8094 0.3720 0.9357 0.8818 0.9627 0.7857 0.9524 0.8635 0.3457	0.0113 0.0145 0.0204 0.0232 0.0003 0.0011 0.0001 0.0154 0.0134 0.0145 0.0136 0.0003	0.7754  0.8215  0.7457  0.7459  0.6486  0.3089  0.7425  0.7457  0.8151  0.7326  0.7638	0.0364 0.0336 0.0115 0.0118 0.0006 0.0010 0.0011 0.0112 0.0325 0.0135 0.0115
A6A2B  A6A2B  I (Bil	LSTM-GS)  PLSR  RF  KNNR  LSTM  SVR  BiLSTM  LSTM-GS)  PLSR  RF  KNNR  LSTM	0.9521 0.7547 0.9538 0.8094 0.3720 0.9357 0.8818 0.9627 0.7857 0.9524 0.8635 0.3457	0.0145 0.0204 0.0232 0.0003 0.0011 0.00154 0.0134 0.0145 0.0136 0.0003	0.8215 0.7457 0.7459 0.6486 0.3089 0.7425 0.7457 0.8151 0.7326 0.7638	0.0336 0.0115 0.0118 0.0006 0.0010 0.0001 0.0112 0.0325 0.0135 0.0115
A6A2B  I (Bil	PLSR  RF  KNNR  LSTM  SVR  BiLSTM  LSTM-GS)  PLSR  RF  KNNR  LSTM	0.7547 0.9538 0.8094 0.3720 0.9357 0.8818 0.9627 0.7857 0.9524 0.8635 0.3457	0.0204 0.0232 0.0003 0.0011 0.0001 0.0154 0.0134 0.0145 0.0136 0.0003	0.7457 0.7459 0.6486 0.3089 0.7425 0.7457 0.8151 0.7326 0.7638	0.0115 0.0118 0.0006 0.0010 0.0001 0.0112 0.0325 0.0135 0.0115
A6A2B  A6A2B  I (Bi)	RF KNNR LSTM SVR BiLSTM LSTM-GS) PLSR RF KNNR LSTM	0.9538 0.8094 0.3720 0.9357 0.8818 0.9627 0.7857 0.9524 0.8635 0.3457	0.0232 0.0003 0.0011 0.0001 0.0154 0.0134 0.0145 0.0136 0.0003	0.7459 0.6486 0.3089 0.7425 0.7457 0.8151 0.7326 0.7638	0.0118 0.0006 0.0010 0.0001 0.0112 0.0325 0.0135 0.0115
A6A2B  A6A2B  I (Bil	KNNR LSTM SVR BILSTM LSTM-GS) PLSR RF KNNR LSTM	0.8094 0.3720 0.9357 0.8818 0.9627 0.7857 0.9524 0.8635 0.3457	0.0003 0.0011 0.0001 0.0154 0.0134 0.0145 0.0136 0.0003	0.6486 0.3089 0.7425 0.7457 0.8151 0.7326 0.7638	0.0006 0.0010 0.0001 0.0112 0.0325 0.0135
A6A2B  A6A2B  I (Bil	SVR  SVR  BiLSTM  LSTM-GS)  PLSR  RF  KNNR  LSTM	0.3720 0.9357 0.8818 0.9627 0.7857 0.9524 0.8635 0.3457	0.0011 0.0001 0.0154 0.0134 0.0145 0.0136 0.0003	0.3089 0.7425 0.7457 0.8151 0.7326 0.7638	0.0010 0.0001 0.0112 0.0325 0.0135
A6A2B  I (Bil	SVR BiLSTM LSTM-GS) PLSR RF KNNR LSTM	0.9357 0.8818 0.9627 0.7857 0.9524 0.8635 0.3457	0.0001 0.0154 0.0134 0.0145 0.0136 0.0003	0.7425 0.7457 0.8151 0.7326 0.7638	0.0001 0.0112 0.0325 0.0135 0.0115
A6A2B	BILSTM  LSTM-GS)  PLSR  RF  KNNR  LSTM	0.8818 0.9627 0.7857 0.9524 0.8635 0.3457	0.0154 0.0134 0.0145 0.0136 0.0003	0.7457 0.8151 0.7326 0.7638	0.0112 0.0325 0.0135 0.0115
A6A2B	LSTM-GS)  PLSR  RF  KNNR  LSTM	0.9627 0.7857 0.9524 0.8635 0.3457	0.0134 0.0145 0.0136 0.0003	0.8151 0.7326 0.7638	0.0325 0.0135 0.0115
A6A2B  I (Bil	PLSR RF KNNR LSTM	0.7857 0.9524 0.8635 0.3457	0.0145 0.0136 0.0003	0.7326 0.7638	0.0135 0.0115
A6A2B  I (Bil	RF KNNR LSTM	0.9524 0.8635 0.3457	0.0136 0.0003	0.7638	0.0115
A6A2B  I (Bil	KNNR LSTM	0.8635 0.3457	0.0003		
A6A2B  I (Bil	LSTM	0.3457		0.6745	0.0006
I (Bil			0.0011		
(Bil	SVR	0.9356		0.3159	0.0010
(Bil		0.,,,,,,,	0.0001	0.7021	0.0001
	BiLSTM	0.8847	0.0135	0.7326	0.0145
	LSTM-GS)	0.9547	0.0121	0.8025	0.0184
	PLSR	0.9324	0.0221	0.7831	0.0318
	RF	0.9421	0.0181	0.7902	0.0221
A7	KNNR	0.8325	0.0002	0.7188	0.0005
	LSTM	0.3453	0.0011	0.3145	0.0010
	SVR	0.9478	0.0001	0.7126	0.0001
J	BiLSTM	0.8824	0.0112	0.7621	0.0332
(Bil	LSTM-GS)	0.9354	0.0181	0.7541	0.0423
	PLSR	0.7625	0.0201	0.7357	0.0185
	RF	0.9524	0.0145	0.7625	0.0136
	KNNR	0.8725	0.0002	0.7012	0.0005
A7B	LSTM	0.3852	0.0010	0.3025	0.0009
	SVR	0.9524	0.0001	0.7212	0.0001
]	BiLSTM	0.8856	0.0124	0.7627	0.0103
(Bi	LSTM-GS)	0.9457	0.0118	0.8225	0.0147
	PLSR	0.7644	0.0201	0.7325	0.0133
		0.9623	0.0115	0.7221	0.0115
A7A2	RF	0.004.5		0.7223	0.0005
	RF KNNR	0.8316	0.0002		

TABLE 4 Continued

Input variable	Modeling method	$R_C^2$	$RMSE_c$	$R_P^2$	RMSE <sub>p</sub>
	SVR	0.9670	0.0001	0.8569	0.0001
	BiLSTM	0.8835	0.0118	0.7326	0.0108
	(BiLSTM-GS)	0.9533	0.0221	0.8225	0.0223
	PLSR	0.7856	0.0214	0.7315	0.0115
	RF	0.9514	0.0124	0.7216	0.0135
	KNNR	0.8354	0.0002	0.7235	0.0005
A7A2B	LSTM	0.2963	0.0012	0.2215	0.0011
	SVR	0.9554	0.0001	0.7956	0.0001
	BiLSTM	0.8824	0.0152	0.7456	0.0125
	(BiLSTM-GS)	0.9623	0.0203	0.8213	0.0263
	PLSR	0.7634	0.0202	0.7301	0.0103
	RF	0.9621	0.0135	0.7214	0.0124
	KNNR	0.8025	0.0003	0.6270	0.0006
A8	LSTM	-0.0046	0.0014	-0.0100	0.0017
	SVR	0.9622	0.0001	0.8297	0.0001
	BiLSTM	0.8812	0.0145	0.7432	0.0115
	(BiLSTM-GS)	0.9615	0.0201	0.8323	0.0154
	PLSR	0.7425	0.0200	0.6524	0.0223
	RF	0.9515	0.0045	0.7545	0.0094
	KNNR	0.8195	0.0003	0.7054	0.0005
A8B	LSTM	0.2952	0.0013	0.1854	0.0012
	SVR	0.9554	0.0001	0.7951	0.0001
	BiLSTM	0.8826	0.0115	0.7225	0.0125
	(BiLSTM-GS)	0.9626	0.0225	0.8245	0.0126
	PLSR	0.7123	0.0200	0.6824	0.0228
	RF	0.9635	0.0045	0.7621	0.0094
	KNNR	0.8157	0.0003	0.6910	0.0005
A8A2	LSTM	0.2441	0.0013	0.1847	0.0011
	SVR	0.9671	0.0001	0.8593	0.0001
	BiLSTM	0.8812	0.0123	0.7456	0.0128
	(BiLSTM-GS)	0.9565	0.0233	0.8245	0.0217
	PLSR	0.7236	0.0196	0.6926	0.0216
	RF	0.9618	0.0043	0.7413	0.0078
	KNNR	0.8821	0.0003	0.6215	0.0006
A8A2B	LSTM	0.3521	0.0013	0.2854	0.0011
	SVR	0.9514	0.0001	0.7852	0.0001
	BiLSTM	0.8884	0.1406	0.8241	0.1592
	(BiLSTM-GS)	0.9624	0.2198	0.8651	0.1652

TABLE 5 Lopex1993 vegetation data model test.

Modeling method	$R_C^2$	$RMSE_c$	$R_P^2$	RMSE <sub>p</sub>
PLSR	0.9657	20.9183	0.8469	28.6118
RF	0.9883	12.2336	0.6527	26.9993
KNNR	0.9631	0.6779	0.7734	0.0585
SVR	0.7911	0.3566	0.6688	0.8384
BiLSTM	0.8824	0.0112	0.7621	0.0332
(BiLSTM-GS)	0.9259	0.0407	0.8503	0.0656

across 400–1000 nm, demonstrating superior convergence and computational efficiency compared to traditional methods, consistent with recent trends in combining optimization algorithms with attention mechanisms (Lang et al., 2024). To effectively capture key yield-related physiological traits and minimize redundancy, we selected SAVI, MSAVI, NDRE, and SIPI as the optimal vegetation indices through random forest regression (Wang et al., 2024; Tooley et al., 2024).

The model's superior performance stems from a strategic data fusion of feature bands, vegetation indices, and Ginkgo canopy region of interest pixel (ROP) sets, an approach consistent with established research (Ceriani et al., 2025). The BiLSTM-GS component particularly outperformed traditional methods due to its ability to capture bidirectional contextual dependencies in spectral sequences, a capability aligned with established mechanistic principles (Zhang et al., 2025). Comparative analysis shows our results exceed in apple yield prediction ( $R_P^2$  =0.78) but trail in corn silage monitoring (>90%), highlighting the cropspecific nature of model performance (Burglewski et al., 2024).

While promising results have been achieved, this study has several limitations: limited generalizability due to single-site validation, the high computational demands of the BiLSTM-GS model, and the time-consuming manual ROI extraction. Future work should prioritize: 1) multi-site and multi-temporal validation to assess model robustness; 2) model lightweighting through compression techniques; 3) automated ROI extraction using deep learning; 4) multi-modal data fusion with LiDAR and meteorological data; 5) applying explainable AI methods to bridge the gap between model performance and biological insight; and 6) integrating various vegetation indices (e.g., TVI, MCARI, MTVI, NDI) to leverage their complementarity for enhancing the model's characterization of multidimensional vegetation physio-biochemical traits.

In conclusion, while the proposed framework shows strong innovation and performance, addressing these limitations through integrated approaches will be crucial for its operational adoption in precision forestry and agriculture.

#### 4 Conclusion

In this study, an innovative method based on hyperspectral imaging technology ( $400 \sim 1000$  nm spectral range) was proposed to realize the non-destructive yield prediction of Ginkgo biloba leaves by

integrating canopy spectral data and measured yield values. Through the systematic evaluation of five spectral preprocessing methods (MSC, SG, SNV, FD, SS), SNV was determined as the optimal preprocessing scheme and used as the basis for subsequent model training. PSO, PSAMA, SPA, PCA, LASSO and CARS algorithms were used for feature selection, and 10, 20, 10, 21, 20 and 23 characteristic wavelengths were extracted respectively. Additionally, the most representative SAVI, MSAVI, NDRE and SIPI vegetation indices were selected from the seven candidate indices by random forest regression analysis. The SNV- (SAVI - MSAVI - NDRE - SIPI - ROP) - (BiLSTM-GS) prediction model is constructed by innovatively fusing the Region of Interest Pixel (ROP) data, and the BiLSTM is optimized by Grid SearchCV (learning rate: 0.01, Hidden layers: 50). The model showed a prediction accuracy of  $R_c^2 = 0.9422$  (RMSE<sub>c</sub> = 0.0817) for the calibration set performance index and  $R_P^2 = 0.8795$  (RMSE<sub>0</sub> = 0.1021) for the prediction set result, thus establishing a robust technical framework for the non-destructive yield assessment of ginkgo planting.

#### Data availability statement

The raw data supporting the conclusions of this article will be made available by the authors, without undue reservation.

#### **Author contributions**

ZZ: Conceptualization, Writing - review & editing, Project administration, Investigation, Methodology, Writing - original draft. MZ: Investigation, Writing - review & editing, Methodology, Funding acquisition, Resources, Project administration, Writing original draft. LQ: Writing - original draft, Methodology, Software, Writing - review & editing, Conceptualization, Resources, Project administration, Investigation, Funding acquisition. BW: Funding acquisition, Writing - review & editing, Methodology, Software, Formal analysis, Project administration, Resources, Writing original draft, Conceptualization, Investigation. HZ: Writing review & editing, Investigation, Writing - original draft, Validation, Project administration. WX: Writing - original draft, Project administration, Investigation, Methodology, Writing - review & editing. QY: Methodology, Project administration, Writing original draft, Investigation, Writing - review & editing. CZ: Investigation, Writing - review & editing, Writing - original draft, Project administration. KZ: Methodology, Writing - review & editing, Writing - original draft, Investigation.

#### **Funding**

The author(s) declare financial support was received for the research and/or publication of this article. We extend our heartfelt gratitude to the following funding sources: Jiangsu Agriculture Science and Technology Innovation Fund (CX (23) 1027), STI2030-Major Projects (2023ZD0405605), Jinpu Research Institute Research Special Funds Project (No.319610001), Jiangsu Innovation and Entrepreneurship

Training Program for College Students(No.202410298131Y), Metasequoia Faculty Research Initiation Fee Project (No.163040193), National Natural Science Foundation of China (NSFC) Project (No.32402209), Jiangsu Forestry Science and Technology Innovation and Promotion Project (LYKJ(2024)05), Frontier Technologies R&D Program of Jiangsu (grant numbers BF2024060).

#### Acknowledgments

We would like to sincerely thank Tang Hao, Meng He, and Hongqian Zhuo from Jiangsu Xuzhou Changrong Agricultural Development Company Limited.

#### Conflict of interest

The authors declare that the research was conducted in the absence of any commercial or financial relationships that could be construed as a potential conflict of interest.

#### References

Andrei, G. Y., Costa, E. M., Anjos, L. H. C. D., and Marcondes, R. A.T. (2023). Enhancing soil mapping with hyperspectral subsurface images generated from soil lab vis-swir spectra tested in Southern Brazil. *Geoderma Reg.* 33, e00641–e00641. doi: 10.1016/j.geodrs.2023.e00641

Black, D., Gill, J., Xie, A., Liquet, B., Di leva, A., Stummer, W., et al. (2024). Deep learning-based hyperspectral image correction and unmixing for brain tumor surgery. *iScience* 27, 111273–111273. doi: 10.1016/j.isci.2024.111273

Bing, L., Jun, S., Ning, Y., Xiao-hong, W., and Xin, Z. (2018). Prediction of Tea Diseases Based on Fluorescence Transmission Spectrum and Texture of Hyperspectral Image. Spectroscopy and Spectral Analysis 39, 2515–2521. 10.3964/j.issn.1000-0593 (2019)08-2515-07

Burglewski, N., Srinivasagan, S., Ketterings, Q., Aardt, V, and J. (2024). Spatial and spectral dependencies of maize yield estimation using remote sensing. *Sensors* 24, 3958–3958. doi: 10.3390/s24123958

Ceriani, R., Brocco, S., Monica, P., Oggioni, S., Vacchiano, G., Motta, R., et al. (2025). Hyperspectral and lidar space-borne data for assessing mountain forest volume and biomass. *Int. J. Appl. Earth Obs Geoinf* 141, 104614–104614. doi: 10.1016/j.jag.2025.104614

Chitra, S., Chaudhry Muhammad, M. A., and Paliwal, J. (2022). Classification of pulse flours using near-infrared hyperspectral imaging. *LWT* 154, 112799–112799. doi: 10.1016/j.lwt.2021.112799

Faehn, C., Konert, G., Keinänen, M., Karppinen, K., and Krause, K. (2024). Advancing hyperspectral imaging techniques for root systems: a new pipeline for macro- and microscale image acquisition and classification. *Plant Methods* 20, 171–171. 10.1186/s13007-024-01297-x

Ge, Y., Atefi, A., Zhang, H., Chenyong Miao, C., Raghuprakash,, Ramamurthy, K., et al. (2019). High-throughput analysis of leaf physiological and chemical traits with vis–nir–swir spectroscopy: A case study with a maize diversity panel. *Plant Methods* 15, 1–12. doi: 10.1186/s13007-019-0450-8

Gila, D. M. M., Martínez, D. B., Satorres Martínez, S., Marchal, P. C., and García, J. G. (2024). Non-invasive detection of pesticide residues in freshly harvested olives using hyperspectral imaging technology. *Smart Agric. Technol.* 9, 100644–100644. doi: 10.1016/j.atech.2024.100644

Jin, X., Han, K., Zhao, H., Wang, Y., Chen, Y., and Yu, J. L. (2023). Detection and coverage estimation of purple nutsedge in turf with image classification neural networks. *Pest Manag Sci.* 80, 2352–0094. doi: 10.1002/ps.8055

Jong, L. J. S., Post, A. L., Geldof, F., Dashtbozorg, B., Ruers, T. J. M., and Sterenborg, H. J. C. M. (2024). Separating Surface Reflectance from Volume Reflectance in Medical Hyperspectral Imaging. *Diagnostics* 14, 1812–1812. 10.3390/diagnostics14161812

Lang, H., Bao, W., Feng, W., Qu, K., Ma, X., and Zhang, X. (2024). Hyperspectral and multispectral images fusion based on pyramid swin transformer. *Infrared Phys. Technol.* 143, 105617–105617. doi: 10.1109/IGARSS53475.2024.10642087

#### Generative AI statement

The author(s) declare that no Generative AI was used in the creation of this manuscript.

Any alternative text (alt text) provided alongside figures in this article has been generated by Frontiers with the support of artificial intelligence and reasonable efforts have been made to ensure accuracy, including review by the authors wherever possible. If you identify any issues, please contact us.

#### Publisher's note

All claims expressed in this article are solely those of the authors and do not necessarily represent those of their affiliated organizations, or those of the publisher, the editors and the reviewers. Any product that may be evaluated in this article, or claim that may be made by its manufacturer, is not guaranteed or endorsed by the publisher.

Li, H., Liu, P., Li, Z., Xu, C., Pan, J., Zhou, Y., et al. (2024). Valorization ofginkgo bilobaleaf powder as a substrate in king oyster mushroom ( Pleurotus eryngii ) cultivation. *Life* 14, 639–639. doi: 10.3390/life14050639

Li, M., Yin, H., Gu, F., Duan, Y., Zhuang, W., Han, K., et al. (2025). Recent advances and applications of nondestructive testing in aaricultural products: A review. *Processes* 13, 2674–2674. doi: 10.3390/pr13092674

Liang, M., Wang, Z., Lin, Y. Li, C., Zhang, L., and Lin, Y. (2024). Study on detection of pesticide residues in tobacco based on hyperspectral imaging technology. *Front. Plant Sci.* 15. doi: 10.3389/fpls.2024.1459886

Liu, Y., Huawei, X., Zhang, Y., Che, F., Shen, N., and Cui, Y. (2022). Leaves, seeds and exocarp of ginkgo biloba L. (Ginkgoaceae): A comprehensive review of traditional uses, phytochemistry, pharmacology, resource utilization and toxicity. *J. Ethnopharmacol* 298, 115645–115645. doi: 10.1016/j.jep.2022.115645

Long, T., Tang, X., Liang, C., Wu, B., Huang, B., Lan, Y., et al. (2024). Detecting bioactive compound contents in dancong tea using vnir-swir hyperspectral imaging and krr model with a refined feature wavelength method. *Food Chem.* 460, 140579–140579. doi: 10.1016/j.foodchem.2024.140579

Lu, F., Jiayi, S., Zhang, G., Nie, F., Wang, J., and Dai, X. (2024). Protective effect of ginkgobiloba (Ginkgoaceae family) leaf extracts on female drosophila melanogaster suffering from ultraviolet irradiation through activating the keap1-nrf2 signaling pathway. *Biol. Bull.* 51, 518–529. doi: 10.1007/s00299-013-1397-2

Mao, B., Cheng, Q., Chen, L, Duan, F., Sun, X., Li, Y., et al. (2024). Multi-random ensemble on partial least squares regression to predict wheat yield and its losses across water and nitrogen stress with hyperspectral remote sensing. *Comput. Electron. Agric.* 222, 109046–109046. doi: 10.1016/j.compag.2024.109046

Marchese, C., Colella, S., Brando, V. E., Zoffoli, M. L., and Volpe, G. (2024). Towards accurate L4 ocean colour products: interpolating remote sensing reflectance via dineof. *Int. J. Appl. Earth Obs Geoinf* 135, 104270–104270. doi: 10.1016/j.jag.2024.104270

Matinfar, M. M., Mohammdi, M. B., and Karami, M. (2025). Unmasking the brain in cocaine use disorder: A deep learning approach with graph convolutional networks and principal component analysis. *Next Res.* 2, 100304–100304. doi: 10.1016/j.nexres.2025.100304

Miettinen, I., Zhang, C., Alonso, L., Marín, B. F., Plazaola, J. G., Grebe, S., et al. (2024). Hyperspectral imaging reveals differential carotenoid and chlorophyll temporal dynamics and spatial patterns in scots pine under water stress. *Plant Cell Environ.* 48, 1535–1554. doi: 10.1111/pce.15225

Nikzad, M. H., Rarani, M. H., and Rasti, R. (2025). Long-short-term memory (Lstm)-based modeling of the stiffness of 3d-printed pla parts. *Mater. Lett.* 379, 137636–137636. doi: 10.1016/j.matlet.2024.137636

Qin, A., Sun, J., Zhu, X., Li, M., Li, C., Wang, L., et al. (2025). The yield estimation of apple trees based on the best combination of hyperspectral sensitive wavelengths algorithm. *Sustainability* 17, 518–518. doi: 10.3390/su17020518

Ren, C., Xu, Q., Meng, Z., and Pan, J. S. (2024). Surrogate-assisted fully-informed particle swarm optimization for high-dimensional expensive optimization. *Appl. Soft Comput.* 167, 112464–112464. doi: 10.1016/j.asoc.2024.112464

- Satyabrata, D., Sujata, C., Giri, N. C., Agyekum, E. B., and AboRas, K. M. (2024). Minimum noise fraction and long short-term memory model for hyperspectral imaging. *Int. J. Comput. Int. Sys* 17, 1–22. doi: 10.1007/s44196-023-00370-y
- Sen, D., Jain, S. K., Rathee, S., Umesh Patil, K. U.K., and Pandey, V. (2025). Comprehensive insights into pathophysiology of alzheimer's disease: herbal approaches for mitigating neurodegeneration. *Curr. Alzheimer Res.* 21, 625–648. doi: 10.2174/0115672050309057240404075003
- Settembre, G., Taggio, N., Buono, N. D., Esposito, F., Lauro, P., and Aiello, A. (2025). A land cover change framework analyzing wildfire-affected areas in bitemporal prisma hyperspectral images. *Math. Comput. Simul* 229, 855–866. doi: 10.1016/j.matcom.2024.10.034
- Shezhou, L., Cheng, W., Xi, X., Pan, F., Qian, M., and Peng, D. (2015). Retrieving aboveground biomass of wetland phragmites australis (Common reed) using a combination of airborne discrete-return lidar and hyperspectral data. *Int. J. Appl. Earth Obs Geoinf* 58, 107–117. doi: 10.1016/j.jag.2017.01.016
- Shi, Y., Wang, F., Xie, H., Fan, B., Li, L., Kong, Z., et al. (2024). Model for prediction of pesticide residues in soybean oil using partial least squares regression with molecular descriptors selected by a competitive adaptive reweighted sampling algorithm. *Agric. Commun.* 2, 100053–100053. doi: 10.1016/j.agrcom.2024.100053
- Song, H., Mehdi, S. R., Wan, Q., Li, Z., Li, M., Wang, M., et al. (2025). Compact staring-type underwater spectral imaging system utilizing K-nearest neighbor-based interpolation for spectral reconstruction. *Opt Laser Technol.* 181, 111880–111880. doi: 10.1016/j.optlastec.2024.111880
- Souza, L. L. D., Candeias, D. N. C., Moreira, E. D. T., Diniz, P. H.G.D., Springer, V. H., Fernandes, D. D. S., et al. (2025). Uv–vis spectralprint-based discrimination and quantification of sugar syrup adulteration in honey using the successive projections algorithm (Spa) for variable selection. *Chemometr Intell. Lab.* 257, 105314–105314. doi: 10.1016/j.chemolab.2024.105314
- Srivastava, P. K., Gupta, M., Singh, U., Prasad, R., Pandey, P. C., Raghubanshi, A. S., et al. (2020). Sensitivity analysis of artificial neural network for chlorophyll prediction using hyperspectral data. *Environ. Dev. Sustain* 23, 1–16. doi: 10.1007/s10668-020-00827-6
- Stevens, C. L., Adriaans, G. M. C., Spooren, C. E. G. M., Peters, V., Pierik, M. J., Weersma, R. K., et al. (2025). Exploring diet categorizations and their influence on flare prediction in inflammatory bowel disease, using the sparse grouped least absolute shrinkage and selection operator method. *Clin. Nutr.* 47, 212–226. doi: 10.1016/j.clnu.2025.02.027
- Sun, M., Yang, Y., Li, S., Yin, D., Zhong, G., and Cao, L. (2024). A study on hyperspectral soil total nitrogen inversion using a hybrid deep learning model cbiresnet-bilstm. *Chem. Biol. Technol. Agric.* 11, 157–157. doi: 10.1186/s40538-024-00681-y
- Sun, X., Zhang, B., Dai, M., Jing, C., Ma, K., Tang, B., et al. (2024). Accurate irrigation decision-making of winter wheat at the filling stage based on uav hyperspectral inversion of leaf water content. *Agr Water Manag* 306, 109171–109171. doi: 10.1016/j.agwat.2024.109171
- Tian, J., Xu, S., Wu, Y., Shi, Y., Duan, Y., Li, Z., et al. (2025). Authenticating vintage in white tea: appearance-taste-aroma-based three-in-one non-invasive anticipation. *Food Res. Int.* 199, 115394–115394. doi: 10.1016/j.foodres.2024.115394

- Tooley, E.G., Nippert, J. B., and Ratajczak, Z. (2024). Evaluating methods for measuring the leaf area index of encroaching shrubs in grasslands: from leaves to optical methods, 3-D scanning, and airborne observation. *Agr For. Meteorol* 349, 109964–109964. doi: 10.1016/j.agrformet.2024.109964
- Tougas, G., Wallis, C. I.B., Lalibert, E., and Vellend, M. (2025). Hyperspectral imaging has a limited ability to remotely sense the onset of beech bark disease. *Remote Sens. Ecol. Conserv.* 64, 199–209. doi: 10.1002/rse2.70013
- Vitor, D. A. C., Soliani, A. G., and Cerutti, S. M. (2023). Standardized extract of ginkgo biloba treatment and novelty on the weak encoding of spatial recognition memory in rats. *Learn. Mem* 30, 85–95. doi: 10.1101/lm.053755.123
- Wan, S., Yang, H., Lin, J., Li, J., Wang, Y., and Chen, X. (2024). Improved whale optimization algorithm towards precise state-of-charge estimation of lithium-ion batteries via optimizing lstm. *Energy* 310, 133185–133185. doi: 10.1016/j.energy.2024.133185
- Wang, J., Chen, C., Wang, J., Yao, Z., Wang, Y., Zhao, Y., et al. (2024). Ndvi estimation throughout the whole growth period of multi-crops using rgb images and deep learning. *Agron* 15, 63–63. doi: 10.3390/agronomy15010063
- Wang, X., Han, J., Liu, C., and Feng, T. (2024). Non-destructive assessment of apple internal quality using rotational hyperspectral imaging. *Front. Plant Sci.* 15. doi: 10.3389/fpls.2024.1432120
- Wang, J, Chen, C, and Wang, J. (2024). Ndvi estimation throughout the whole growth period of multi-crops using rgb images and deep learning. *Agron* 15, 63–63. doi: 10.3390/agronomy15010063
- Wei, Y., Hu, H., Xu, H., and Mao, X. (2024). Identification of chrysanthemum variety via hyperspectral imaging and wavelength selection based on multitask particle swarm optimization. *Spectrochim Acta A* 322, 124812–124812. doi: 10.1016/j.saa.2024.124812
- Xu, P., Fu, L., Pan, Y., Chen, D., Yang, S., and Yang, R. (2024). Identification of maize seed vigor based on hyperspectral imaging and deep learning. *Bulletin of the National Research Centre* 48, 84–84. 10.1186/s42269-024-01239-6
- Xueyu, T., Yanjie, L., Yan, W., Wang, M., Tan, Z., Jiang, J., et al. (2021). Heritable variation in tree growth and needle vegetation indices of slash pine (Pinus elliottii) using unmanned aerial vehicles (Uavs). *Ind. Crops Prod* 173, 114073–114083. doi: 10.1016/j.indcrop.2021.114073
- Xunlan, L., Fangfang, P., Zhaoxin, W., Guohui, H., and Jianfei, L. (2023). Non-destructive detection of protein content in mulberry leaves by using hyperspectral imaging. Frontiers in Plant Science 14, 1275004–1275004. 10.3389/fpls.2023.1275004
- Yan, K., Song, X., Yang, J., Xiao, J., Xu, X., Guo, J., et al. (2025). Citrus huanglongbing detection: A hyperspectral data-driven model integrating feature band selection with machine learning algorithms. *Crop Prot* 188, 107008–107008. doi: 10.1016/j.cropro.2024.107008
- Yue, J., Wang, J., Zhang, Z., Li, C., Yang, H., Feng, H., et al. (2024). Estimating crop leaf area index and chlorophyll content using a deep learning-based hyperspectral analysis method. *Comput. Electron. Agric.* 227, 109653–109653. doi: 10.1016/j.compag.2024.109653
- Zhang, S., Chen, B., Chen, C., Hovorka, M., Qi, J., Hu, J., et al. (2025). Myoelectric signal and machine learning computing in gait pattern recognition for flat fall prediction. *Med. Novel Technol. Devices* 25, 100341–100341. doi: 10.1016/j.medntd.2024.100341